

LATERAL DIVERGENCE IN HIGH POWER LASER DIODES: METHOD OF
ANALYSIS FOR ASSESSING CONTRIBUTING FACTORS

by

Nicholas A. Vail

Copyright © Nicholas A. Vail 2019

A Thesis Submitted to the Faculty of the

COLLEGE OF OPTICAL SCIENCES

In Partial Fulfillment of the Requirements

For the Degree of

MASTER OF SCIENCE

In the Graduate College

THE UNIVERSITY OF ARIZONA

2019

THE UNIVERSITY OF ARIZONA
GRADUATE COLLEGE

As members of the Master's Committee, we certify that we have read the thesis prepared by *Nicholas Vail*, titled *Lateral Divergence in High Power Laser Diodes: Method of Analysis for Assessing Contributing Factors* and recommend that it be accepted as fulfilling the dissertation requirement for the Master's Degree.



Mahmoud Fallahi

Date: Aug 13, 2019



Stanley Pau

Date: Aug 13, 2019




Mark Crowley

Date: Aug 13 2019

Final approval and acceptance of this thesis is contingent upon the candidate's submission of the final copies of the thesis to the Graduate College.

I hereby certify that I have read this thesis prepared under my direction and recommend that it be accepted as fulfilling the Master's requirement.



Mahmoud Fallahi
Master's Thesis Committee Chair
Optical Sciences

Date: Aug. 13, 2019

ARIZONA

Contents

1	ABSTRACT	5
2	INTRODUCTION	6
2.1	AIMS AND MOTIVATION	6
2.2	THESIS STRUCTURE.....	7
3	BACKGROUND THEORY	8
3.1	INTRODUCTION	8
3.2	SEMICONDUCTOR LASER FUNCTION	8
3.2.1	<i>Absorption.....</i>	8
3.2.2	<i>Emission types</i>	8
3.2.3	<i>Optical feedback</i>	9
3.2.4	<i>Optical gain</i>	9
3.2.5	<i>Threshold condition</i>	10
3.3	NON-RADIATIVE PROCESSES	11
3.3.1	<i>Band-to-band recombination</i>	11
3.3.2	<i>Phonon-assisted recombination.....</i>	11
3.3.3	<i>Trap-assisted recombination</i>	11
3.4	SEMICONDUCTOR LASER CHARACTERISTICS THAT AFFECT DIVERGENCE.....	12
3.4.1	<i>Temperature dependence.....</i>	12
3.4.2	<i>Mode types</i>	12
3.4.3	<i>External pumping.....</i>	13
3.4.4	<i>Mode guiding techniques</i>	13
3.4.5	<i>Optical confinement</i>	15
3.5	CARRIER-INDUCED CHANGES OF REFRACTIVE INDEX.....	15
3.5.1	<i>Band filling</i>	15
3.5.2	<i>Bandgap shrinkage</i>	15
3.5.3	<i>Free-carrier absorption</i>	16
3.6	SPECIAL CONSIDERATIONS FOR QUANTUM WELLS	16
3.7	FABRICATION PROCESSES FOR LASER DIODE STRUCTURES	17
3.7.1	<i>Double mesa</i>	19
3.7.2	<i>Single mesa with a tapered contact</i>	20
3.7.3	<i>Double mesa with a tapered contact.....</i>	22
3.8	SUMMARY	23
4	TESTING AND CHARACTERIZATION OF LASER DIODES	24
4.1	INTRODUCTION	24
4.2	EXPERIMENTAL SETUP.....	24
4.2.1	<i>Equipment.....</i>	24
4.2.2	<i>Devices tested</i>	24
4.3	LIGHT CURRENT VOLTAGE TESTING.....	25
4.3.1	<i>Procedure</i>	25
4.3.2	<i>Results.....</i>	25
4.4	NEAR FIELD CHARACTERIZATION	27
4.4.1	<i>Procedure</i>	27
4.4.2	<i>Results.....</i>	27
4.5	FAR FIELD CHARACTERIZATION.....	29
4.5.1	<i>Procedure</i>	29
4.5.2	<i>Results.....</i>	30
4.6	LATERAL BEAM PARAMETER PRODUCT.....	34
4.7	TEMPERATURE EFFECT ANALYSIS	35
4.7.1	<i>Wavelength shift due to temperature variation.....</i>	35
4.7.2	<i>Heat generation calculation</i>	36
4.8	SPECTRAL MAPPING.....	38
4.8.1	<i>Tool design.....</i>	38
4.8.2	<i>Relating the image to the thermal gradient</i>	39

4.8.3	<i>Lateral mode progression analysis</i>	40
4.9	HAKKI-PAOLI TEST APPLICATION	44
4.9.1	<i>Purpose of Hakki-Paoli test</i>	44
4.9.2	<i>Applying the Hakki-Paoli method</i>	44
4.9.3	<i>Spectral mapper application to Hakki-Paoli</i>	45
4.9.4	<i>Internal loss</i>	48
4.10	PHASE CHANGE TO MEASURE REFRACTIVE INDEX.....	49
4.11	SUMMARY	51
5	MODELLING OF KNOWN STRUCTURE	53
5.1	INTRODUCTION	53
5.2	CREATING THE MODEL FROM STRUCTURE DETAILS	53
5.3	RESULTS FROM CORE WIDTH VARIATION WITH INCREASED MODES	54
5.4	USING LASERMOD TO FIND REFRACTIVE INDEX CHANGES	58
5.5	SUMMARY	59
6	SUMMARY	61
6.1	ACHIEVEMENTS.....	61
6.1.1	<i>Testing and characterization</i>	61
6.1.2	<i>Modelling and simulations</i>	62
6.2	FUTURE WORK	62
7	APPENDIX	64
7.1	MATLAB SCRIPT FOR HAKKI-PAOLI METHOD	64
7.2	FULL MODEL SIMULATION RESULTS.....	69
8	REFERENCES	74

1 Abstract

Lateral far field blooming or slow axis divergence is a common problem of high-power diode lasers and there are many different factors that contribute. Some of the major factors include temperature, carrier-induced effects, high order modes, mode types, and optical confinement. In this study, these properties were characterized and quantified in order to build a model to assess and simulate lateral divergence. A novel device called a spectral mapper was built to separate out lateral and longitudinal modes and their changes as current is varied. The collected and calculated data was input into LaserMOD, where simulations were run to determine the extent to which core width, mode number and refractive index changes modify the divergence of the device. While the modelling software was unable to support large numbers of modes due to weak confinement and also underestimated refractive index change in multimodal devices, the model and simulations were still able to quantify that more modes led to more lateral divergence. These tests and models can be used to improve coupling performance and hopefully provide insight into how high-power laser diodes can be further integrated with fiber lasers.

2 Introduction

In this thesis, characterization methods for laser diodes were performed on three different structure types to compare how the vertical structure and gain guiding techniques would affect the slow axis divergence. Using a unique method to separate the lateral and longitudinal modes, the effects of many lateral and longitudinal modes and thermal lensing effects were able to be included as factors contributing to slow axis divergence. This information was used with LaserMOD modelling software to help model, simulate and understand the effects of many lateral modes.

This work was necessary because high power diode lasers suffer from many lateral modes, as well as carrier and thermal effects that are not present in high speed telecommunications lasers. Therefore, it was necessary to understand and characterize these effects and their relation to divergence so high-power lasers can continue to be developed and improved so better coupling performance and integration into fiber can be achieved.

2.1 Aims and motivation

Lateral far field blooming or slow axis divergence is a common problem of high-power diode lasers. Many different studies have shown that changes of refractive index and lateral thermal profiles are contributing causes, as well as high order lateral modes (1-7). Changes in the refractive index profile will change either the waveguide dimensions or cause a change at established barriers that would improve or weaken the total internal reflection of the waveguide. Additionally, carrier induced effects that change the absorption of the material, such as band gap shrinkage, band filling, and free carrier absorption, have all been shown to cause changes in the refractive index (8). The absorption is related to the refractive index, as shown by the Kramers-Kronig relation. Because absorption and gain are directly related to each other, it was important to measure the gain spectrum of the laser and subsequently determine the internal loss. Using a method described by Hakki and Paoli (9), the threshold modal gain was measured and internal loss was determined for use with the LaserMOD model and other calculations. The changes of refractive index due to interband transitions and intraband excitations using the Drude model were also calculated and have been measured experimentally by observing the phase change of the laser spectrum (10).

Thermal effects cause a lateral heat profile across the laser diode which results in a slight change in refractive index, creating a thermal lens, or a gradient refractive index profile across the laser (11). Hotspots are created by lateral modes and can cause a thermal profile to fluctuate. It has been observed that an increase in lateral modes, which create more thermal profile changes, can lead to an increase in lateral divergence (12). This thesis attempts to identify these effects and has developed a technique to measure the longitudinal modes of the laser cavity allowing for the thermal profile and lateral modes to be seen and to effectively measure the thermal lens and change in lateral divergence.

2.2 Thesis structure

This thesis is organized into 3 sections: background theory of laser diodes, the testing procedures and results, and finally the modelling and simulation of the laser diode using LaserMOD. The testing and characterization include a full characterization on beam characteristics for 768 nm laser diodes, including light current voltage (LIV) tests, near-field and far-field analyses, and threshold modal gain and internal loss calculations. The trends in these data are correlated to the physical structure of the laser diode, as well as underlying mechanisms. The modelling and simulations include incorporation of the epitaxial structure and a two-dimensional cross-section geometry, model setup using data collected in the characterization and fabrication processes, as well as results comparing the model generated simulations and the general trends observed in the characterization of actual devices.

3 Background theory

3.1 Introduction

This chapter will be used to introduce concepts of semiconductor lasers that are relevant to the work being presented in the following chapters. The first section describes basic principles of semiconductor laser function, including absorption, emission, optical feedback, gain and threshold conditions. The next sections discuss factors that contribute to divergence in these laser diodes, including non-radiative processes, temperature dependence, mode types, mode guiding, optical confinement, and carrier-induced changes of refractive index. A brief explanation of quantum wells and fabrication processes are then discussed.

3.2 Semiconductor laser function

Changes in the creation of photons is described by several different terms which are important for understanding the fundamental workings of semiconductor laser diodes, namely absorption, emission, feedback and gain.

3.2.1 Absorption

Absorption occurs when a photon stimulates an electron to move from the lower energy level of the valence band to the higher energy level of the conduction band. When a photon with more energy than the band gap passes through the semiconductor, there is a high probability that the photon will be absorbed, expending its energy to an electron in the valence band raising the electron to the conduction band.

3.2.2 Emission types

Emission can occur in two different ways: spontaneous and stimulated. Spontaneous emission is when an electron moves from the conduction band to the valence band. In this process a photon is generated that corresponds to the energy bandgap of the material. Stimulated emission, also known as radiative recombination, is when there is a higher amount of spontaneous emission, stimulating the combining of an electron hole pair. This process generates another photon that will have the same characteristics of the photon that initiated the combination (13). Stimulated emission creates photons that have the same energy and momentum as the initiating (or incident) photon. For stimulated emission to overcome absorption, the separation of the quasi-Fermi levels must be greater than the photon energy (14).

3.2.3 Optical feedback

Optical feedback is obtained by using flat mirrors at the ends of the cavity to create a Fabry Perot cavity, enabling the confinement of more photons. The reflectivity of the mirrors can be calculated with Fresnel's equation,

$$R = \left| \frac{n_1 - n_2}{n_1 + n_2} \right|^2$$

which allows calculation of the reflection (R) at the interface of two materials with different indices of refraction (n_1, n_2). However, the amount of reflection from the semiconductor-air interface is small. Additionally, using this method means that the front and rear facets of the laser have the same amount of reflection and light will escape the cavity in equal amounts from the front and rear. Therefore, it is better to use a thin film process to create a high reflectivity mirror at the rear surface and an anti-reflectivity mirror at the front surface. This ensures that most of the light will leave through the front mirror. This is an improved method of optical feedback, which does require more processing than simply using the cleaved surfaces with an air interface. Optical feedback serves two goals: first, providing directional selectivity by only reflecting photons moving along its axis, and second, providing wavelength selectivity because feedback will be stronger for wavelengths corresponding to the longitudinal modes of the cavity (14). It is important to note that efficient optical feedback lowers the threshold level so that the number of photons in the cavity increases more quickly, allowing the laser to move to stimulated emission faster. This can lower the amount of loss by not losing as many photons at the mirror surfaces of the cavity.

3.2.4 Optical gain

Optical gain is the process that occurs when a photon stimulates an electron to transition from a higher energy state to a lower state. This recombination of an electron and hole causes a photon to be generated. This photon has the same properties as the original photon such as wavelength, polarization and direction of travel. The condition for optical gain is when the stimulated emission rate is greater than the absorption rate. Any change in gain is associated with a change in refractive index, as described by the Kramer-Kronig relation, which will subsequently result in a change in waveguide properties (8, 10, 15, 16).

An important aspect of gain is population inversion. Population inversion is when the material has an applied voltage, moving holes and electrons into a small area. To create gain

in a semiconductor the condition of population inversion described by the Bernard-Duraffourg condition must be met. Where E_g is the energy of the bandgap, E_{Laser} is the energy of the laser output, and E_{FC} and E_{FV} are the quasi-Fermi levels of the conduction and valence bands respectively.

$$E_g < E_{Laser} < E_{FC} - E_{FV}$$

This occurs when the materials on either side of the quantum well become p or n doped, creating more holes or electrons in the material. The p-n junction of semiconductor material becomes forward biased. This shifts the conduction and valence bands bringing them closer together between the p and n type materials. The Fermi level also experiences a shift under forward bias. The resulting shifts create overlap of electrons and holes in the n and p type materials respectively where recombination can occur. Population inversion can increase the amount of gain because of the increase in opportunity for recombination.

3.2.5 Threshold condition

When the optical gain of a cavity is greater than the loss, the threshold condition is met. The threshold condition is when the gain mechanisms are equal to the loss mechanisms. At this point, spontaneous emission transitions into stimulated emission, which then becomes the dominant source of photon generation and narrows the spectral width. Stimulated emission must compete against absorption processes where an electron hole pair is created by absorbing a photon. While the electron population in the valence band is greater than the population in the conduction band, absorption is the dominant process. When the applied current reaches the threshold condition, there will be more electrons in the conduction band allowing spontaneous emission to trigger stimulated emission and overcome absorption loss. Once the threshold current is exceeded and this transition occurs, its output power will increase linearly with current. The material becomes optically transparent at this point allowing for photons to travel through the cavity, which allows the laser to emit coherent light. Threshold current density depends on the optical mode confinement and can vary with the thickness of the active region and length. The threshold current is higher for weakly index guided devices compared to strongly index guided devices because of weaker mode confinement and increased carrier diffusion. Non-radiative recombination also leads to an increase of the threshold current (14).

3.3 Non-radiative processes

Auger recombination is a non-radiative process which involves four particle states such as three electrons and one hole, or two electrons and two holes, etc. The energy released during electron hole recombination is transferred to another electron or hole, which is then excited to a higher energy state in the band. The electron or hole relaxes to a state of thermal equilibrium emitting the energy as a phonon. Three different types of auger recombination can occur: band-to-band, phonon-assisted and trap-assisted (14).

3.3.1 Band-to-band recombination

Band-to-band recombination has three different mechanisms. The first mechanism is when an electron recombines with a hole in the heavy hole valence band and the extra energy is transferred to another electron in the conduction band, causing it to move to an excited state then relax back to thermal equilibrium and lose energy to phonons. The other two band-to-band processes are very similar. The second process involves an electron from the conduction band recombining with a heavy hole band and the extra energy from an electron in the split off band recombining with a heavy hole. The third involves an electron from the light hole band recombining with a hole from the heavy hole band. Band-to-band auger recombination mechanisms can be reduced by low operating temperature and by creating a large band gap (14).

3.3.2 Phonon-assisted recombination

Phonon-assisted auger processes use the momentum of the phonon to eliminate the minimum energy requirement of band-to-band transitions. Due to coulomb interactions, a heavy hole is in an intermediate state. When recombination occurs, the phonon interacts with the heavy hole in the intermediate state allowing it to move to its final state in the heavy hole band (14).

3.3.3 Trap-assisted recombination

Trap-assisted auger processes occur at defects (which are also known as traps), which create a continuum of states, allowing for electrons and holes near the defects to recombine non-radiatively. Defects in the active region are grown during the epitaxial process. These defects can propagate during operation. Additionally, at cleaved facets or other surfaces exposed to the environment, dangling bonds form bonds with impurities. This creates a large number of defects on the surface allowing trap-assisted non-radiative recombination (14). By refining the epitaxial process, defects can be minimized inside the structure and at surfaces or facets

that are exposed to the environment. For instance, a common method to remove dangling bonds with impurities is to strip and coat the cleaved facets in a vacuum.

3.4 Semiconductor laser characteristics that affect divergence

Divergence is the angle at which the coherent light exits the cavity, or how the beam spreads as light is emitted. There are several laser characteristics that affect divergence, namely, temperature dependence, modes, external pumping, and cavity characteristics.

3.4.1 Temperature dependence

Temperature is included in the Fermi factors and thus affects the distribution of electrons and holes in the conduction and valence bands. At high temperatures, the carriers are distributed over a wider range, reducing the maximum gain (14). Temperature changes the location of the wavelength of the maximum gain of the material, or the center wavelength. As the gain shifts, the index of refraction changes proportionally to the emitting wavelength of the material. The heat distribution is not uniform across the surface of the laser and will be higher in the center and taper out towards the edges of the laser surface. This is because the primary lateral modes of the laser create the largest confinement of carriers to the center of the cavity, which means that is where the greatest opportunity for non-radiative recombination occurs. This thermal lensing effect and subsequent change in index of refraction changes the divergence angle (6).

Controlling temperature is important because changes in temperature can cause changes in the Fermi level, which is related to many factors, including the band gap of the material, the optical gain and the divergence of the beam due to thermal lensing (14).

3.4.2 Mode types

There are several different types of modes – longitudinal, lateral, and transverse.

Longitudinal modes are created by the reflections back and forth from the rear to the front of the cavity. The cavity's resonance frequency is related to the longitudinal mode of the Fabry-Perot cavity. Due to inhomogeneous broadening, multiple longitudinal modes are present.

While the mode spacing ($\Delta\nu$) can be found from the following equation:

$$\Delta\nu = \frac{c}{2\mu_g L}$$

the refractive index of the active region changes as the frequency changes. To use the equation, the speed of light constant (c), the group refractive index (μ_g) and the length of the cavity (L) are needed. To account for these changes in refractive index the group index of the material needs to be used. Longitudinal modes can be related to the gain profile of the laser (14).

The lateral modal field is parallel to the junction plane of the laser. Guiding of the lateral mode can be done through gain- and index-guiding because of possible changes in optical gain and refractive index. For strong index-guiding, the lateral change in the refractive index must be much greater than the refractive index of the active region. If only a change in the effective refractive index is used for guiding and lateral mode control, then gain-guiding is being used. Lateral modes can be found by solving waveguide equations using index of refraction changes. The lateral modes can be used to find a normalized waveguide width, which is then used to find the lateral confinement factor. It has been observed that an increase in lateral modes can lead to an increase in lateral divergence (6, 12, 17, 18).

The transverse modal field is perpendicular to the junction plane of the laser. Guiding of the transverse mode is done through index guiding because of the change in refractive index between the active region and the cladding or waveguide layer. Transverse modes are related to the waveguide materials and dimensions vertically using a slab-waveguide model (14).

3.4.3 External pumping

The refractive index changes with the pumping of current into a semiconductor laser, which is a form of external pumping. This is due to the high density of charge carriers in the active region of the device. The concentration of charge carriers leads to the shrinking of the band gap also contributing to the change in refractive index, which can influence the waveguide (14).

3.4.4 Mode guiding techniques

Semiconductor laser cavities can be gain- or index-guided depending on the mechanisms varying the optical gain or index of refraction used to confine the lateral modes.

Gain of the active region (g) can be calculated with the material absorption constant ($\text{Im}(\chi_0)$), the external pumping susceptibility constant ($\text{Im}(\chi_p)$), the vacuum wave number ($k_0 = 2\pi/\lambda$) and the refractive index of the medium without any external effects (μ_b).

$$g = -\frac{k_0}{\mu_b} \text{Im}(\chi_0 + \chi_p)$$

Gain guiding is done by directing the flow of current into a smaller region of the active area, through contact strip geometries. This allows for changes in the effective refractive index. The changes come about because of carrier density. The variation in optical gain that this creates is what causes confinement of lateral modes. When the optical mode distribution is controlled by the optical gain, it is a gain-guided structure (14, 19, 20).

Gain-guided lasers exhibit a specific characteristic. A kink in the L-I curve can be indicative of the optical mode moving along the junction plane or a transition to higher order modes. The change in optical mode along the junction plane changes the carrier density in the active region, altering the Fermi energy. The voltage across the diode is equal to the separation of the quasi-Fermi levels so a change in voltage will occur with a change in the optical mode. This appears as a kink in the L-I curve. With a wider contact strip, the kink will occur at lower power (14, 19, 20).

Two different types of index-guiding methods are used commonly; namely weak and strong index-guiding. The difference between the two types is how the active region is confined. Weak index-guiding is done by creating a small change in the effective refractive index, thereby increasing the effective refractive index over a small portion of the width of the active layer in the center of the device. This creates a change in carrier concentration and diffusion. The active region is continuous while the change in effective refractive index is created by varying thickness of cladding layers. The lateral index step is determined by the thickness of the waveguide layer. If the waveguide layer is increased in thickness, the index step becomes smaller. The change of effective refractive index can be created by etching a ridge or channels in the cladding area. Strong index-guiding is done by creating a buried structure. This can be done with multiple epitaxial growth processes or by using an implant technique to change the properties of the material. The active region is bound by lower index layers or higher bandgap materials, both parallel and perpendicular to the active region (14, 19, 20).

3.4.5 Optical confinement

Optical confinement naturally occurs with the different guiding mechanisms because they create a change in the bandgap of the material. A material with a smaller bandgap has a larger refractive index. This allows for a natural waveguide to be formed. The larger refractive index surrounded by a lower index material allows for total internal reflection, confining the light to the active region of the waveguide (13).

3.5 Carrier-induced changes of refractive index

Three carrier-induced effects contribute to change of refractive index: band filling, bandgap shrinkage, and free-carrier absorption. Band filling and free-carrier absorption contribute to a negative change of refractive index, while bandgap shrinkage produces a positive change of refractive index. Depending on the energy of the photon being below or above the bandgap energy, the total effect on the refractive index will be negative or positive (8). High power lasers have high carrier concentration allowing these effects to have a different impact than would be seen in a lower power laser commonly used for telecommunications.

3.5.1 Band filling

The band filling effect is strongest in materials with small effective masses and low energy gaps. The process of band filling occurs when the density of states is low enough that a small number of electrons can fill the band in the lowest energy states, forcing electrons to need more energy to move across the bandgap. This leads to a reduction of the absorption coefficient. The absorption coefficient can be related to the index of refraction using the following equation:

$$n(E) = 1 + \frac{2c\hbar}{e^2} P \int_0^\infty \frac{\alpha(E')}{E'^2 - E^2} dE'$$

where c is the speed of light, e is the electron charge, $E = \hbar\omega$ is the photon energy, and P is the principle value of the integral from the Kramers-Kronig relation (8, 10, 15, 16). This leads to the refractive index decreasing for energies near and below bandgap energy and an increase for energies greater than the bandgap energy. According to Bennett et al., using a photon energy of $\sim 1.65\text{eV}$, band filling effects could have a negative change in refractive index of 0.2 (8).

3.5.2 Bandgap shrinkage

Bandgap shrinkage occurs when the injected electrons occupy the states at the bottom of the conduction band. If the concentration of electrons reaches a large enough value, the electron wave functions overlap, creating a gas of interacting particles. The electrons start to repel

each other due to coulomb forces. This can result in a screening of electrons and a decrease in electron energy, lowering the energy of the conduction band. The effect is similar for holes in the valence band except it increases the energy of the valence band. Both of these effects combine to reduce the bandgap energy. The change in bandgap energy can be related to the change in absorption with the following equation, where c is the speed of light, E_g is the bandgap energy and E is the energy of the photon (as detailed in section 3.5.1):

$$\Delta\alpha(\chi, E) = \frac{c}{E} \sqrt{E - E_g - \Delta E_g(\chi)} - \frac{c}{E} \sqrt{E - E_g}$$

This change can then be related to the refractive index using the previous equation for the absorption coefficient in section 3.5.1, where $\Delta\alpha$ can be inserted as detailed in Bennett et al (8). The change in refractive index is positive for energies below bandgap because of the increase in the absorption coefficient (21).

3.5.3 Free-carrier absorption

Free-carrier absorption occurs when a carrier absorbs a photon and moves to a higher energy state within the band. The Drude model shows that free carrier absorption is proportional to the electron and hole concentration and the square root of the wavelength. Using the following equation,

$$\Delta n = \frac{-6.9 \times 10^{-22}}{nE^2} \left\{ \frac{N}{m_e} + P \left(\frac{m_{hh}^{1/2} + m_{lh}^{1/2}}{m_{hh}^{3/2} + m_{lh}^{3/2}} \right) \right\}$$

the change in refractive index due to free-carrier absorption can be calculated, where n is the background index of refraction, E is the energy of the photon (as described in section 3.5.1), N is the electron density, m_e is the mass of the electrons, P is the whole density, m_{hh} is the mass of heavy holes and m_{lh} is the mass of the light holes (8). Free-carrier absorption is also known as the plasma effect in the Drude model. The change in refractive index will be negative for energies below the bandgap because of the wavelength dependence. When the photon energy is decreased below the bandgap energy, the plasma effect becomes stronger (22, 23).

3.6 Special considerations for quantum wells

When the thickness of the semiconductor material is on the order of the de Broglie wavelength ($\lambda = h/p$), unique properties not typical of bulk material occurs. This leads to the properties of the quantum well (24). The carriers in motion normal to the active layer are

confined to a well. The energy levels in the well are discrete energy levels, similar to a one-dimensional quantum well. The discretized energy levels for the valence band will have heavy and light hole levels for each energy level. The emitting wavelength differs from bulk material systems in that the bandgap energy and the energy from the energy states combine to make up the emitting wavelength of a quantum well laser. The confinement factor for a single quantum well is

$$\Gamma \cong 2\pi^2(n_a^2 - n_c^2) d^2 / \lambda_o^2$$

where n_a and n_c are the refractive indices of the active and cladding layers, d is the active layer thickness, and λ_o is the free space wavelength (14).

The quantum well region may be strained to gain desirable properties, such as a low threshold current density and a lower line width. This is done by slight variations in the lattice constant of the quantum well region to the cladding and substrate. The strain, compressive or tensile, can split the heavy and light hole valence bands. Under compressive strain, the heavy hole valence band becomes the closest to the conduction band, whereas under tensile strain, the light hole valence band separates and moves closer to the conduction band. If the recombination occurs with the heavy hole valence band, then the light being emitted will be transverse electric polarized. If the recombination occurs with the light hole valence band, then the light being emitted will be transverse magnetic polarized. Compressive strain will have a lower threshold current compared to tensile strain (14, 24-26). Strain in any form will cause a change in refractive index because it changes the gain profile.

3.7 Fabrication processes for laser diode structures

The semiconductor laser is grown in a single molecular beam epitaxial growth process. A three-inch diameter gallium arsenide (GaAs) substrate wafer is used to begin the growth process. This is lattice-matched with the material that is grown. A single quantum well is grown between waveguide and cladding layers.

The photolithography process is how the pattern is created on the wafer. The process uses a positive photoresist chemical. The wafer is heated before a primer is applied. The primer will allow the photoresist to adhere to the wafer. The primer is spun onto the wafer for an even distribution. The wafer is then heated again to bake the moisture off of the wafer. After, the

photoresist is applied to the wafer and spun on for an even distribution. Uniformity is important for the exposure step of photolithography. The wafer is baked at a lower temperature to remove excess moisture. The wafer is then taken to a mask aligner to be exposed to ultraviolet light. Using a mask, the photoresist is exposed to the ultraviolet light for a specific amount of time so as not to over or under expose the pattern and alter it from the desired pattern. The wafer is then developed. This will wash away the exposed areas of the photoresist to create a pattern. The amount of time that the wafer is developed is important as this can change the size of the area being washed away in the developer solution. The wafer is rinsed with de-ionized water to stop the developing process. The wafer is then baked at high temperature to harden the photoresist to withstand the etching process.

The wet etching process will create the ridges of the device waveguide. A solution of de-ionized water, phosphoric acid, and hydrogen peroxide is used. The solution is maintained at a constant temperature during the process. Phosphoric acid and hydrochloric acid are also mixed to use for etching. This solution is also maintained at a constant temperature. The wafers are etched with the first solution then rinsed with de-ionized water. The second solution is then used to etch the wafer followed by another rinsing step. This process is then repeated one more time. The photoresist is then removed from the wafer using acetone, which is then removed using de-ionized water.

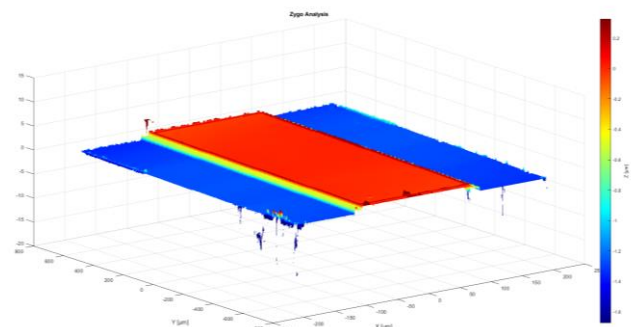
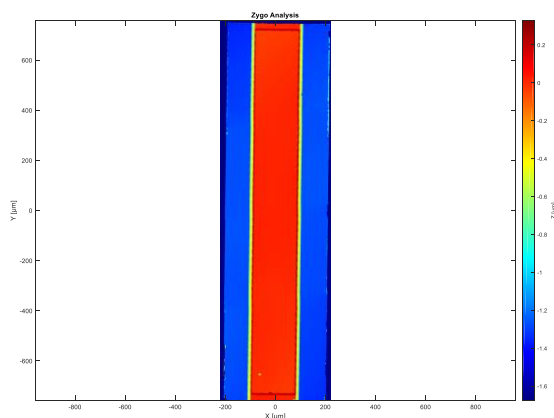
A layer of silicon dioxide (SiO_2) is deposited on top of the etched wafer as a dielectric. This is done by using the process of plasma-enhanced chemical vapor deposition. This allows for a uniform and consistent layer of SiO_2 to be deposited. A contact window is patterned on top of the SiO_2 using the process described earlier. Using a buffer oxide etchant, the contact window is etched away in the SiO_2 . The photoresist is then removed with acetone, which is then removed by rinsing with de-ionized water.

With the contact window opened, the metal layers can be deposited. Using a sputtering method, the metal is deposited on the bottom and top of the wafer. This is done in two different processes because the metal composition is different for the metal in contact with the p-side of the wafer compared to the n-side of the wafer. The thickness of the deposited metal is measured and then polished to the correct thickness. A rapid thermal annealing process is done to allow for the dopants in the contact metal to drift into the semiconductor

metal to create a low resistance barrier between the metal and semiconductor. This will ideally be an ohmic contact.

The following sections contain images of the different devices that were readily available for fabrication. Parameter details for the images in the following sections are as follows. For a double mesa device, the contact opening is 163 microns wide. The width of the first ridge is 178 microns and the width at the bottom of the ridge is 199 microns. Using two different ridge widths creates a stairs effect on the effective refractive index. A smaller contact opening also helps to confine the carriers. The first ridge has a height of approximately 0.74 microns. The second ridge has a height of 0.75 microns. The dielectric layer is approximately 0.22 microns deep. All of these values were as expected for the double ridge style device and were confirmed using a Zygo interferometer. The other double mesa device was similar in ridge height except it used a tapered contact as shown in the figure. The single mesa design used a mesa height of approximately 0.75 microns with a tapered contact. The following figures depict all measurements of the structures. All devices were mounted onto a copper tungsten sub mount using gold tin solder. It is important to note that the gold tin solder is a rigid solder and can cause stress in the laser diode. During packaging of laser diode devices, the strain from soldering the laser diode to a sub mount can cause defects in the laser structure. This creates spots of non-radiative recombination and changes in the polarization of the laser to transverse magnetic from transverse electric. These effects are not accounted for by LaserMOD in the model or simulation but would be important to assess for additional work.

3.7.1 Double mesa



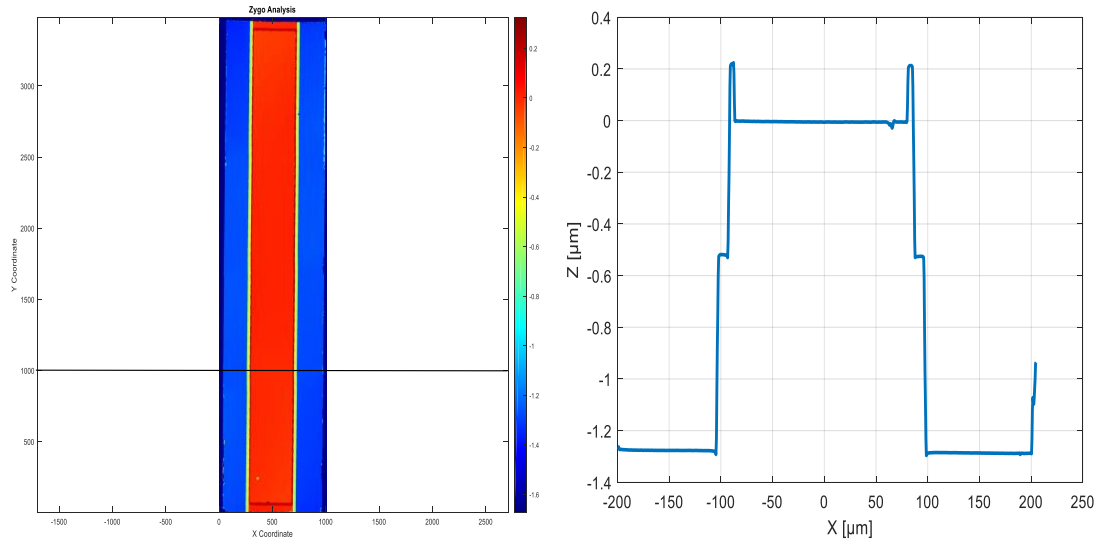
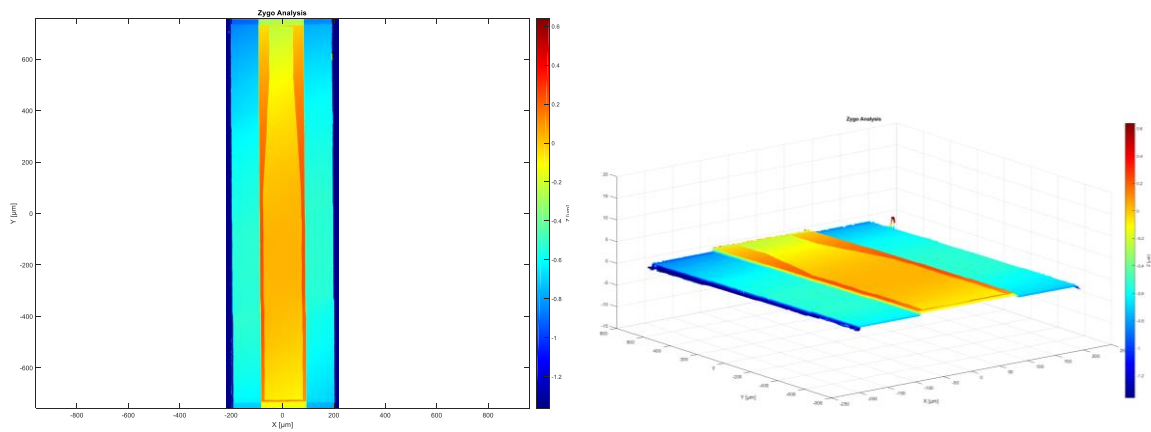


Figure 3.1. These Zygo interferometer images show the double mesa square contact design, which were used to confirm the fabrication process. The top left image shows a top down view, top right shows the side view, bottom left shows the top down view with line showing the position that the ridge structure measurement in the bottom right was taken.

3.7.2 Single mesa with a tapered contact



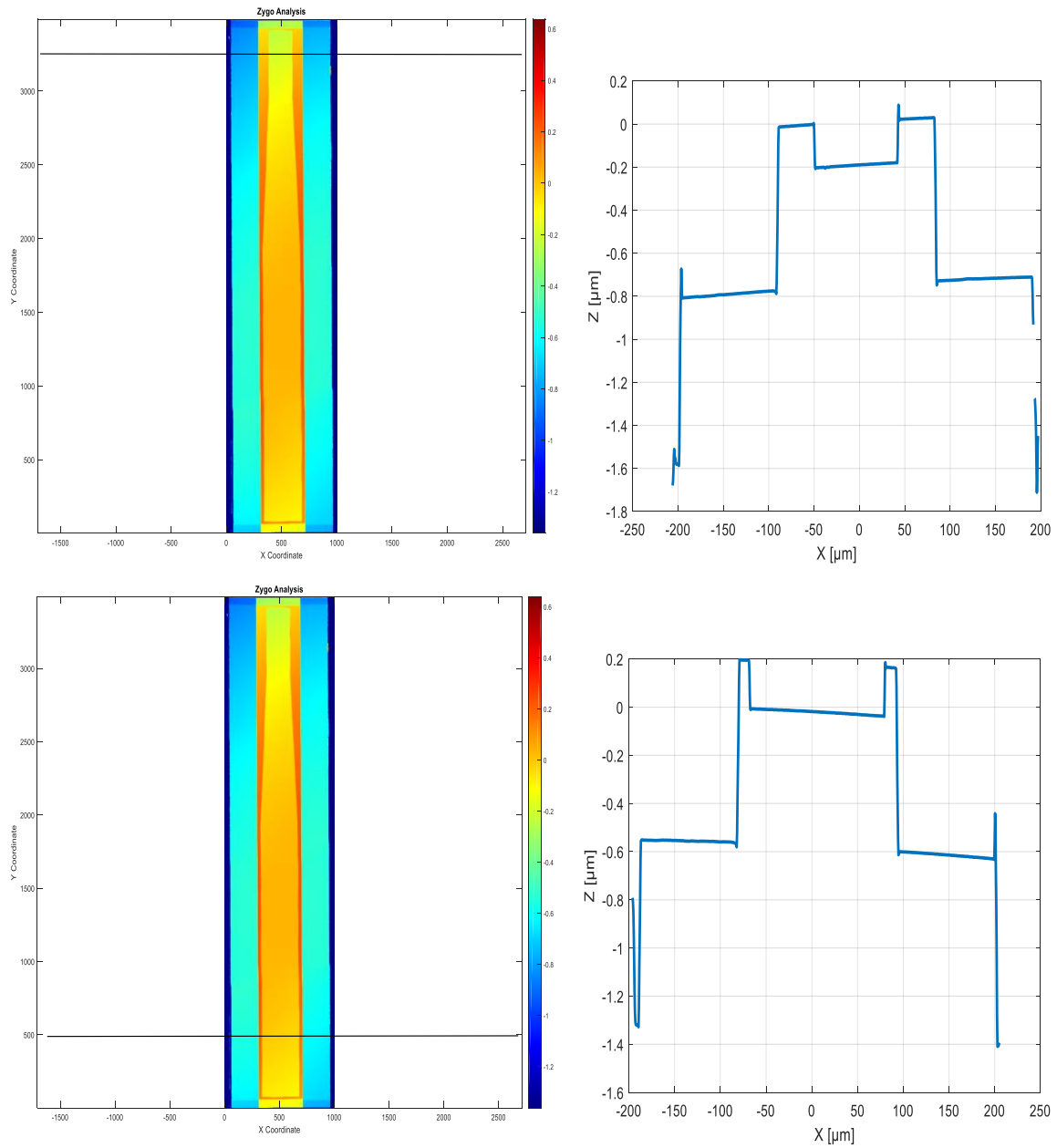


Figure 3.2. These Zygo interferometer images show the single mesa tapered contact design, which were used to confirm the fabrication process. The top left image shows a top down view, top right shows the side view, middle and bottom left show the top down view with lines showing the position that the ridge structure measurements in the middle and bottom right were taken. The tapered contact is apparent when comparing the two ridge structure measurements.

3.7.3 Double mesa with a tapered contact

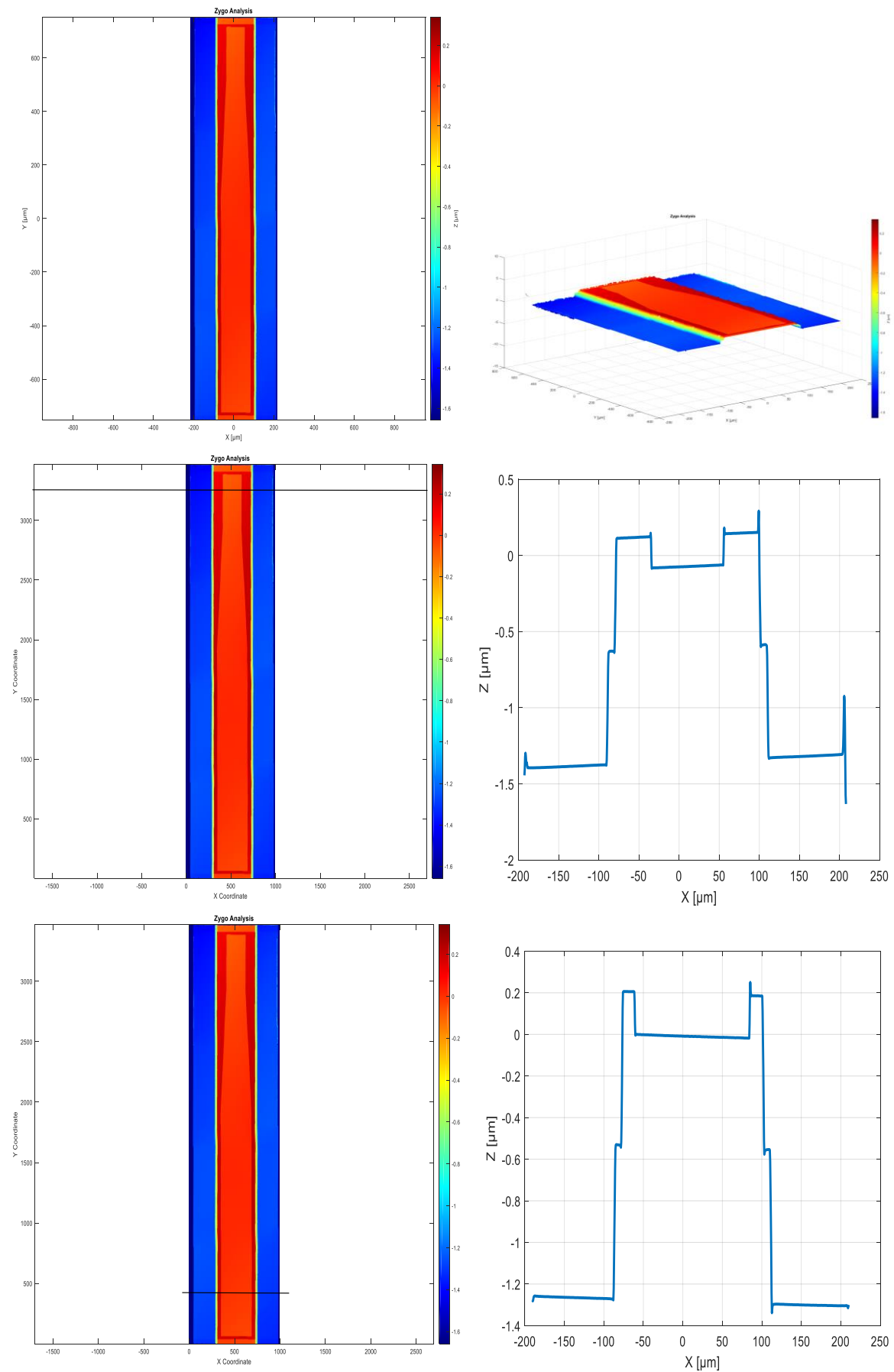


Figure 3.3. These Zygo interferometer images show the double mesa tapered contact design, which were used to confirm the fabrication process. The top left image shows a top down view, top right shows the side view, middle and bottom left show the top down view with lines showing the position that the ridge structure measurements in the middle and bottom right were taken. The tapered contact is apparent when comparing the two ridge structure measurements.

3.8 Summary

These basic principles discussed above are all essential to understanding the effects occurring in the semiconductor laser diode that would change the waveguide properties leading to changes in lateral divergence. The effects discussed that were observed and quantified include temperature dependence and heat generation in section 4.7, mode types and guiding/confinement in section 4.8, the gain and internal loss in section 4.9, and carrier-induced changes of the refractive index in section 5.4.

4 Testing and characterization of laser diodes

4.1 Introduction

In this chapter, procedures and results are discussed for each characterization method for the semiconductor laser diodes. The characterizations performed were light current voltage testing to show the relation between input power and output power, near field characterization to find the beam waist, far field characterization to identify the divergence, lateral beam parameter product to compare the near field and far field of each device, temperature effect analysis, spectral mapping to separate the longitudinal modes and magnify the lateral modes, Hakki-Paoli test to find the gain and internal loss of the semiconductor material, and a method to measure the phase change relative to the change in refractive index.

4.2 Experimental setup

4.2.1 Equipment

All experiments were done using a goniometer stage with a stainless-steel water-cooled mounting system to allow for precision angular movement. The goniometer was controlled using software to ensure repeatability and reliability between measurement sets. A thermoelectric module was sandwiched between the water-cooled section and the plate securing the laser diode assembly. The laser diode assemblies were mounted with hard solder onto copper tungsten heat sinks and were secured to a copper tungsten mount with a plastic cap that applies pressure to the top of the mount. The cap used a spring-loaded pin to contact the p side of the laser diode. The water for cooling the stage was set to 9.9 degrees Celsius and the thermoelectric controller was set to 10 degrees Celsius to maintain the temperature of the copper tungsten at 10 degrees Celsius for all experiments. The Newport temperature controller model 3700 was used to control the thermoelectric module and has precision to 0.01 of a degree. The power supply used was a Newport laser diode driver model 5060 with milliamp precision.

4.2.2 Devices tested

Three different structures were tested and with each structure, ten diodes were evaluated. The first structure was a double mesa with a square contact, the second a single mesa with a tapered contact, and the third a double mesa with a tapered contact. These structures

encompass both index-guiding and gain-guiding mechanisms (14, 20). For each test, all devices for each structure design were initially analysed, but for final comparison, the two most consistent devices for each structure were used.

4.3 Light current voltage testing

4.3.1 Procedure

Light current voltage (LIV) testing was done first to verify that the laser diodes were operating correctly. LIV quantified the device power at current values from 0 to 4 Amps in steps of 0.01. In order to find the gain threshold, straight lines were fitted to the data for the spontaneous emission and stimulated emission. The point where these lines intersect is indicative of the threshold current. The resolution of the LIV testing equipment was sufficient to accurately identify the gain threshold for the current.

4.3.2 Results

LIV output was graphed, as shown in Figure 4.1, where linear best-fit lines were fit to the sections of the power output that were recognizable as spontaneous and stimulated emission. The intersection points, representing the threshold current, for each structure type are detailed in Table 4.1. The threshold current and voltage was similar for all structures, however the tapered contact designs were less efficient than the square contact as seen by the current vs. output power lines in the LIV plots below.

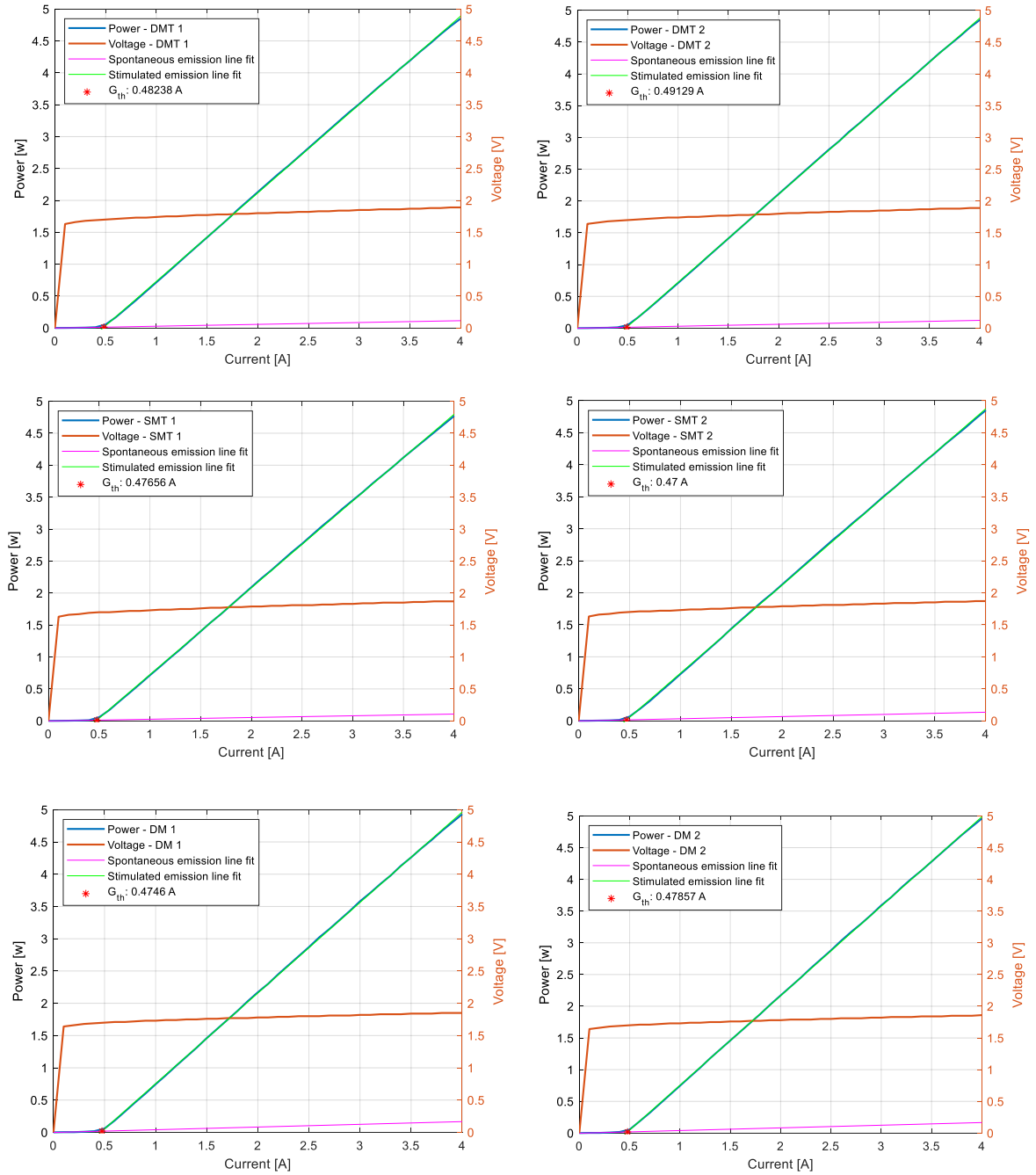


Figure 4.1 These plots depict the light (power in watts), current (Amps) and voltage (volts). The data for the devices are plotted as blue lines for power and orange lines for voltage. The lines fit to the spontaneous and stimulated emissions are in magenta and green respectively. The threshold current was found by finding the intersection of the two emission lines. The first row corresponds to the double mesa tapered contact structure, the second to single mesa tapered contact and the last to the double mesa with square contact.

	Average Threshold Current
Double Mesa	0.4765 A
Single Mesa Tapered contact	0.4732 A
Double Mesa Tapered contact	0.4867 A

Table 4.1 The table shows the average threshold current for the three different structures.

4.4 Near field characterization

4.4.1 Procedure

Near field characterization of the slow-axis propagation was done for all devices. All measurements were done at currents of 0.5, 0.6, 0.7, 0.8, 0.9, 1.0, 1.5, 2.0, 2.5, 3.0, 3.5, and 4.0 Amps. A Nikon plan fluorite 20x objective 0.5 numerical aperture and 2.1 mm working distance was used as part of a custom microscope to image the near field during operation. Due to the high power of the lasers tested, neutral density filters were used to avoid damaging the camera. Additionally, due to the extreme sensitivity of the microscope to vibration and the small depth of field, there were some difficulties capturing these high-resolution images with a camera. This was overcome by using an air-floated optical bench and by using the goniometer stage to ensure that the front facet was square to the microscope objective. These images were processed using a line sum technique over the x-axis for the slow or lateral axis. This was done to capture near field dimensions for calculation of the beam parameter product to compare the different designs and to observe the intensity profile across the front facet of the laser diode.

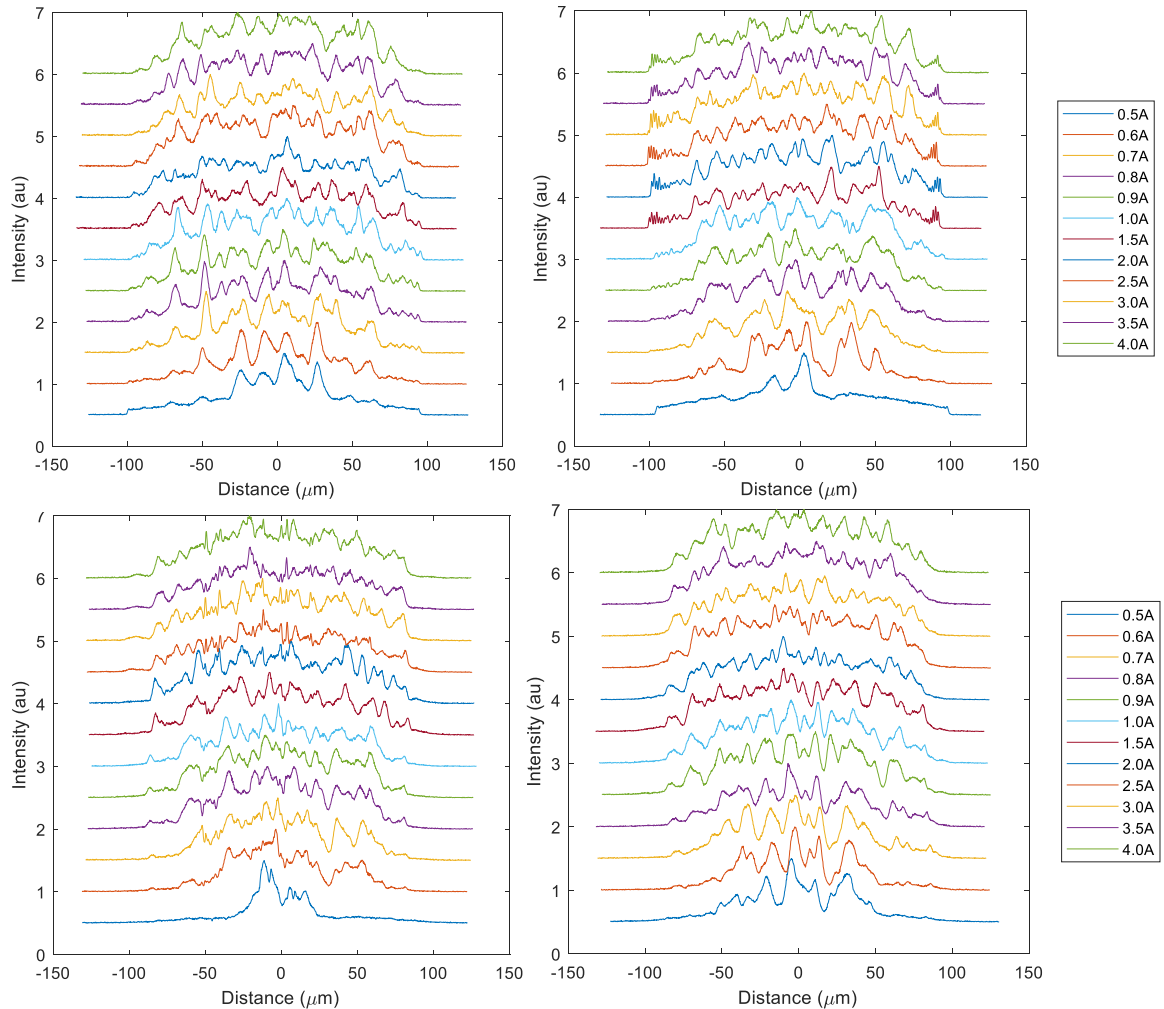
4.4.2 Results

The images in Figure 4.2 show the evolution of the near field with increased current. The peaks in the near field intensity are indicative of lateral modes. The tapered-contact designs started with fewer modes because the current density was higher at the rear of the cavity where the contact is narrower. However, as the current was increased, the current density increased towards the front of the cavity and more modes were supported. With the tapered contact designs, more than half of the double and single mesa devices displayed modal build-up at the edges of the active region, an example of which can be seen in the top right plot in Figure 4.2. At higher currents, the number of modes between the tapered-contact and the regular contact designs became similar. Interestingly, as the current was increased, the object plane seemed to change. This could be due to the emitting facet heating up and flexing slightly. Also interestingly, the highest point of intensity appears to stay in the center with

the tapered contact designs; however, with the square contact, it appears to shift from the center to ± 50 microns once the current exceeds 2 Amps.

It is also interesting and important to note that even between the two most consistent devices of the same structure design, there can be differences in modal distribution. This could be an artifact from fabrication, from packaging-induced stresses or from cleaving the individual laser diodes from the wafer.

From the near field images, values were obtained for the 95% enclosed power and are displayed in Table 4.2. This was used for the calculation of the lateral beam parameter product after the far field analysis.



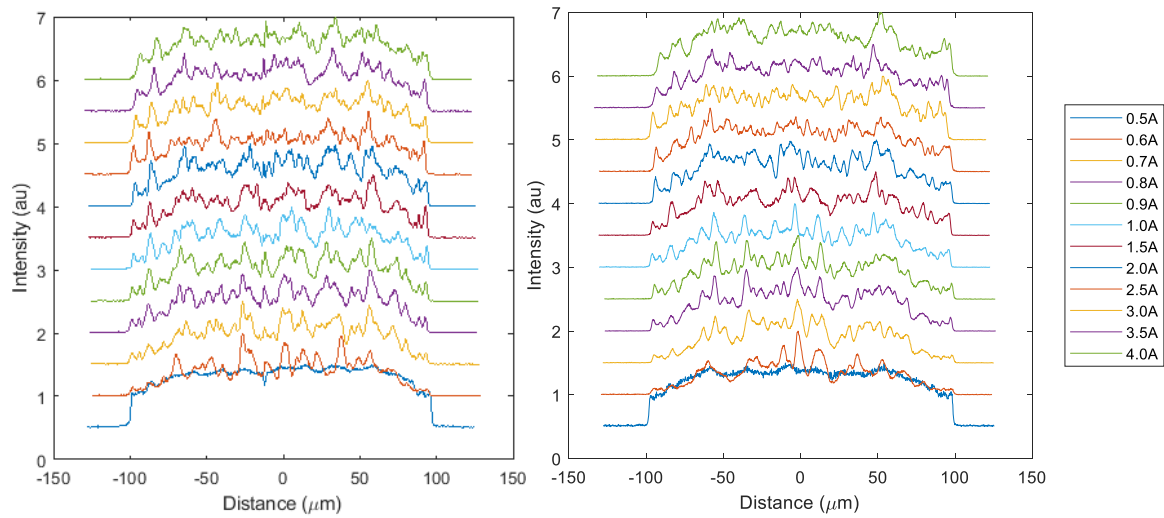


Figure 4.2. A near field for two devices of identical structure is taken for comparison. The intensity of the profile can be seen to evolve as the current is increased between 0.5 Amps and 4 Amps. The first row corresponds to the double mesa tapered contact structure, the second to single mesa tapered contact and the last to the double mesa with square contact. These graphs are of the lateral plane of the emitting facet of the laser.

Current	DM 1	DM 2	DMT 1	DMT 2	SMT 1	SMT 2
0.5A	185.25	181.00	163.74	171.63	149.81	145.40
0.6A	163.73	161.19	145.75	142.60	129.27	139.25
0.7A	166.39	158.30	152.09	140.86	134.77	147.42
0.8A	168.20	161.08	155.18	147.88	140.30	150.09
0.9A	169.22	166.09	160.64	150.13	142.88	151.80
1.0A	169.99	170.00	162.85	153.53	145.11	152.79
1.5A	172.51	171.67	164.09	165.62	156.51	158.29
2.0A	173.10	171.80	161.88	167.57	156.47	154.41
2.5A	176.84	174.44	158.49	166.80	157.67	153.82
3.0A	173.68	175.12	152.54	166.87	156.57	154.68
3.5A	173.64	174.57	153.69	165.40	154.83	150.34
4.0A	174.39	175.83	152.44	164.22	154.68	152.10

Table 4.2. Values for near field lateral width (units are in μm) at 95% enclosed power. DM corresponds to double mesa square contact devices, DMT = double mesa tapered contact and SMT = single mesa tapered contact. These values are used in the calculation of the lateral beam parameter product.

4.5 Far field characterization

4.5.1 Procedure

Far field characterization of the slow-axis and fast-axis propagation was done for all devices. All measurements were done at currents of 0.5, 0.6, 0.7, 0.8, 0.9, 1.0, 1.5, 2.0, 2.5, 3.0, 3.5, and 4.0 Amps. A slit aperture with a baffle tube was used with a silicon avalanche photodetector that was placed 0.5 meters from the emitting facet. For the lateral scan, or

slow-axis, the scanning range was set to ± 20 degrees and the transverse, or fast-axis, scanning range was set for ± 60 degrees allowing for the capture of the entire field. This data was analysed and plotted to observe the intensity profile of the far field. This was also used for calculation of the lateral beam parameter product to compare the different designs.

4.5.2 Results

The slow-axis scan images are included in Figure 4.3 and the fast-axis scan images are included in Figure 4.4. In the fast-axis, the smooth Gaussian shape is indicative of a single mode in the transverse direction of the laser. While in the slow-axis, the shape is still Gaussian, however, the many peaks in the curve are due to multiple modes present in the lateral direction. It is difficult to tell exactly how many lateral modes are present with a far field scan because of the overlap in the emitted light of each mode. Additionally, the double mesa tapered contact design had side lobes in the far field. These could be caused by fabrication stress or because of the modal build-up at the edges of the active region that were observed in the near field slow-axis scans.

The slow-axis full width half max values are shown in Table 4.3 and the fast-axis full width half max values are in Table 4.4. These values were used in creating the LaserMOD simulations and in validating simulation results against the actual model. From the far field scans, values were obtained for the 95% enclosed power and are displayed in Table 4.5. This was used for the calculation of the lateral beam parameter product.

Current	DM 1	DM 2	DMT 1	DMT 2	SMT 1	SMT 2
0.5A	9.16	8.99	2.67	1.72	1.29	2.05
0.6A	8.40	3.22	3.01	2.45	3.99	2.45
0.7A	8.49	4.79	3.72	2.82	4.50	3.55
0.8A	8.70	4.87	5.04	3.31	4.64	4.21
0.9A	8.67	4.07	6.60	3.43	4.89	4.28
1.0A	8.79	6.36	6.68	3.47	5.11	5.34
1.5A	8.88	8.03	7.43	6.71	6.42	6.05
2.0A	9.22	9.23	7.39	6.91	6.15	6.08
2.5A	9.98	10.90	7.33	8.58	8.92	7.70
3.0A	10.74	11.67	6.78	8.19	9.21	8.43
3.5A	9.81	10.98	8.13	5.80	8.97	8.69
4.0A	11.13	11.57	8.11	9.50	9.52	8.78

Table 4.3. The degree values for the slow axis full width half max are shown for the three different structure designs. The values from the double mesa were used as input into the LaserMOD modelling software. DM = double mesa, DMT = double mesa with tapered contact, SMT = single mesa tapered contact. Current was increased from 0.5 Amps to 4 Amps.

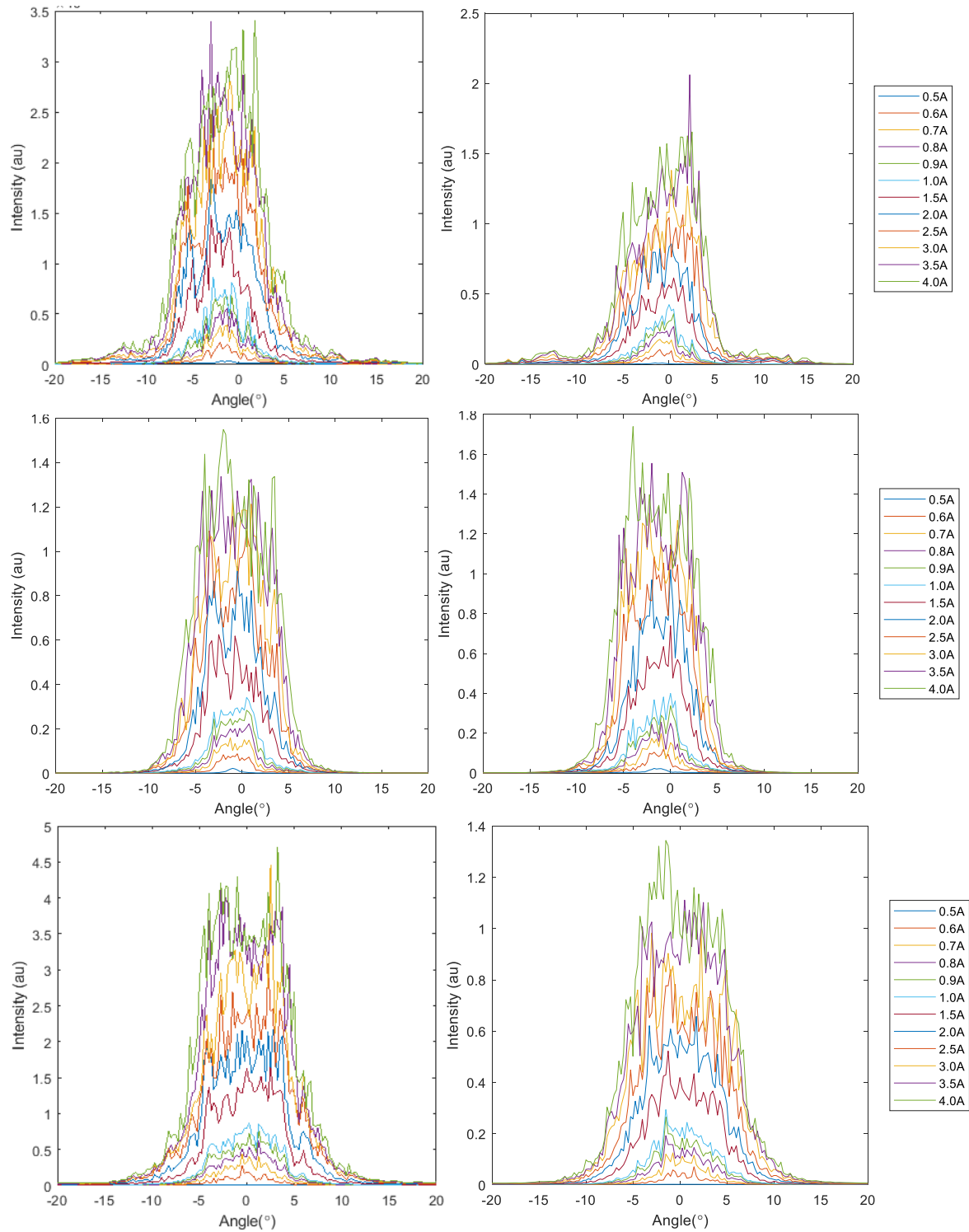
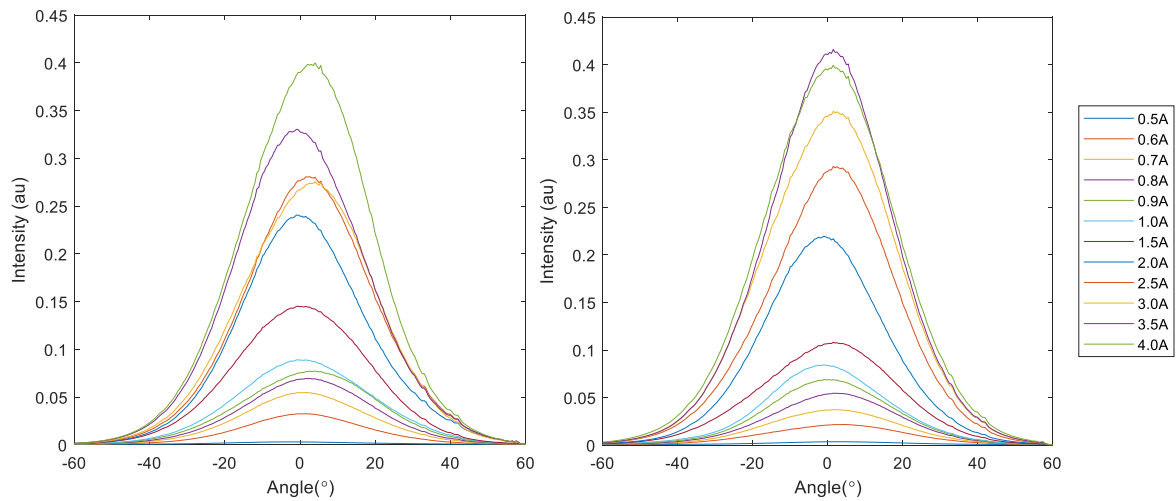


Figure 4.3. Images from the slow axis scans are shown with two devices for each structure type. The first row is the double mesa tapered contact, the second is single mesa tapered contact, the last is the double mesa. It is apparent that even among devices with the same structure, there is variation in the slow axis profile.

Current	DM 1	DM 2	DMT 1	DMT 2	SMT 1	SMT 2
0.5A	29.51	39.95	37.99	40.64	40.64	41.31
0.6A	31.79	38.65	41.61	36.20	39.49	37.03
0.7A	40.10	40.57	40.08	37.63	41.35	38.93
0.8A	41.22	40.37	38.10	38.58	41.08	36.31
0.9A	44.27	40.76	37.38	41.09	40.84	35.41
1.0A	45.68	40.96	35.61	40.79	40.11	36.23
1.5A	42.14	39.82	41.19	41.14	39.49	36.98
2.0A	41.81	39.11	36.39	37.12	38.62	38.39
2.5A	42.60	39.40	37.82	38.14	38.64	37.36
3.0A	40.95	39.00	40.66	40.44	38.58	38.92
3.5A	36.59	38.15	37.14	39.52	40.71	37.90
4.0A	37.73	37.27	40.59	39.18	39.77	38.63

Table 4.4. The degree values for the fast axis full width half max are shown for the three different structure designs. The values from the double mesa were used as input into the LaserMOD modelling software. DM = double mesa, DMT = double mesa with tapered contact, SMT = single mesa tapered contact. Current was increased from 0.5 Amps to 4 Amps.



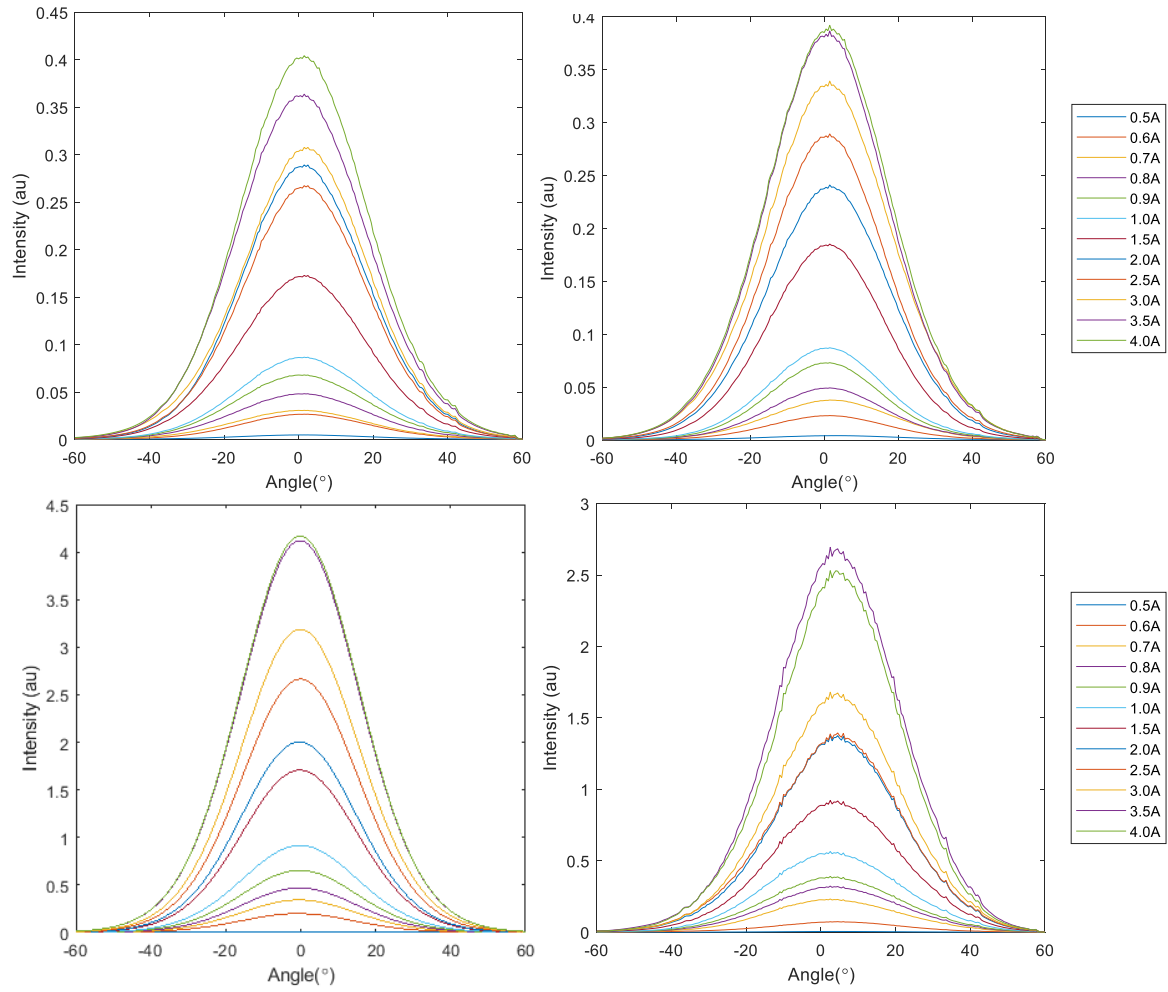


Figure 4.4. Images from the fast-axis scans are shown with two devices for each structure type. The first row is the double mesa tapered contact, the second is single mesa tapered contact, the last is the double mesa. It is apparent that even among devices with the same structure, there is variation in the fast-axis profile as well as the slow-axis.

Current	DM 1	DM 2	DMT 1	DMT 2	SMT 1	SMT 2
0.5A	-	36.24	32.25	34.26	31.34	29.94
0.6A	24.02	26.25	19.86	22.16	18.58	17.99
0.7A	17.55	19.33	14.21	15.45	13.99	13.75
0.8A	15.83	16.23	12.67	13.02	12.78	12.57
0.9A	15.24	15.22	12.12	12.26	12.32	11.95
1.0A	14.86	14.65	12.00	12.25	12.09	11.79
1.5A	15.46	14.53	11.82	16.30	12.10	11.26
2.0A	16.70	15.44	11.62	16.82	11.50	11.34
2.5A	17.84	15.93	11.34	17.57	11.94	11.36
3.0A	17.46	16.66	11.56	18.60	11.94	11.42
3.5A	16.87	16.67	12.09	17.08	12.40	11.86
4.0A	17.20	16.91	12.92	18.89	12.92	12.53

Table 4.5. Values for far field lateral divergence (units are in degrees) at 95% enclosed power. DM corresponds to double mesa square contact devices, DMT = double mesa tapered contact and SMT = single mesa tapered contact. These values are used in the calculation of the lateral beam parameter product. The first measurement for the double mesa (DM 1) was not differentiable from background noise and was therefore excluded.

4.6 Lateral beam parameter product

Using the equation from Winterfeldt 2014, the lateral beam parameter product is calculated (BPP_{lat}), where $w_{95\%}$ is the lateral full beam waist and $\theta_{95\%}$ is the far field angle containing 95% of the power (1). Note that beam waist refers to the narrowest point in the beam, which for a laser diode is the near field.

$$BPP_{lat} = \frac{w_{95\%} \theta_{95\%}}{4}$$

The lateral beam parameter product results are included in Table 4.6. While lateral beam parameter product is a standard measurement of performance for a laser diode used to assess the effectiveness of fiber coupling, by multiplying the beam waist and the far field angle, the beam parameter product can show favoritism for a device that has a narrower beam waist. The single mesa device with the tapered contact has the smallest beam parameter product, but it has the same far field divergence. This is due to the sharp change in effective refractive index confining the light to a smaller width in the near field. The double mesa tapered contact design had inconsistent differences when compared to the double mesa square contact. While the device that did not show modal build-up in the near field slow-axis scan in section 4.4 showed improvement in the lateral beam parameter product, the device that did have modal build up was worse. This shows that the tapered contact does not always offer significant advantage during high-power operation. While it can improve beam characteristics, it is inconsistent and has the potential to be worse than the standard square contact design.

For this reason, the double mesa with the square contact window was chosen for other experiments. The beam characteristics are better for some of the tapered contact devices, but for effective use, efficiency and consistency would need to be improved. More than half of the tapered contact designs suffered from a modal build-up at the edges of the confined active region. These devices have worse beam characteristics than the double mesa square contact. Additionally, there was lateral mode hopping present in the taper contacts because of carrier

density differences between the rear and the front of the cavity. Because this created an extra variable due to mode inconsistency, the square contact window was selected for additional tests.

Current	DM 1	DM 2	DMT 1	DMT 2	SMT 1	SMT 2
0.5A	-	28.61	23.03	25.65	20.48	18.99
0.6A	17.15	18.46	12.63	13.78	10.48	10.93
0.7A	12.74	13.35	9.43	9.49	8.23	8.84
0.8A	11.62	11.41	8.58	8.40	7.82	8.23
0.9A	11.25	11.03	8.49	8.03	7.68	7.91
1.0A	11.02	10.87	8.52	8.21	7.65	7.86
1.5A	11.63	10.88	8.46	11.78	8.26	7.77
2.0A	12.61	11.57	8.20	12.30	7.85	7.64
2.5A	13.76	12.12	7.84	12.78	8.21	7.63
3.0A	13.23	12.73	7.69	13.54	8.16	7.71
3.5A	12.78	12.69	8.10	12.33	8.37	7.78
4.0A	13.09	12.97	8.59	13.53	8.72	8.32

Table 4.6. These are the calculated lateral beam parameter product values in mm*milliradians. The first measurement for the double mesa (DM 1) was not differentiable from background noise and was therefore excluded. DM = double mesa, DMT = double mesa tapered contact, SMT = single mesa tapered contact.

4.7 Temperature effect analysis

4.7.1 Wavelength shift due to temperature variation

Ambient temperature variation was created using the thermoelectric controller during operation at threshold current so there was limited heating by non-radiative recombination or other internal effects that would generate heat. By varying only the ambient temperature, the shift in wavelength was recorded and plotted in Figure 4.5. The result from the data collected showed a wavelength shift of 0.23 nm/K. While efforts were made to ensure that the shift in wavelength was only due to the ambient temperature, there is a possibility that other factors could be contributing to the shift, such as lurking factors altered by the change in ambient temperature or subsequent change in carrier density distribution.

If this experiment were repeated, the power out would need to be measured in parallel to the spectrum so that the generated internal heat could be more thoroughly monitored. This would allow for better control of how the ambient temperature changed the center

wavelength of the spectrum. If changes in heat were created internally, then those could be factored into the temperature-dependent wavelength shift.

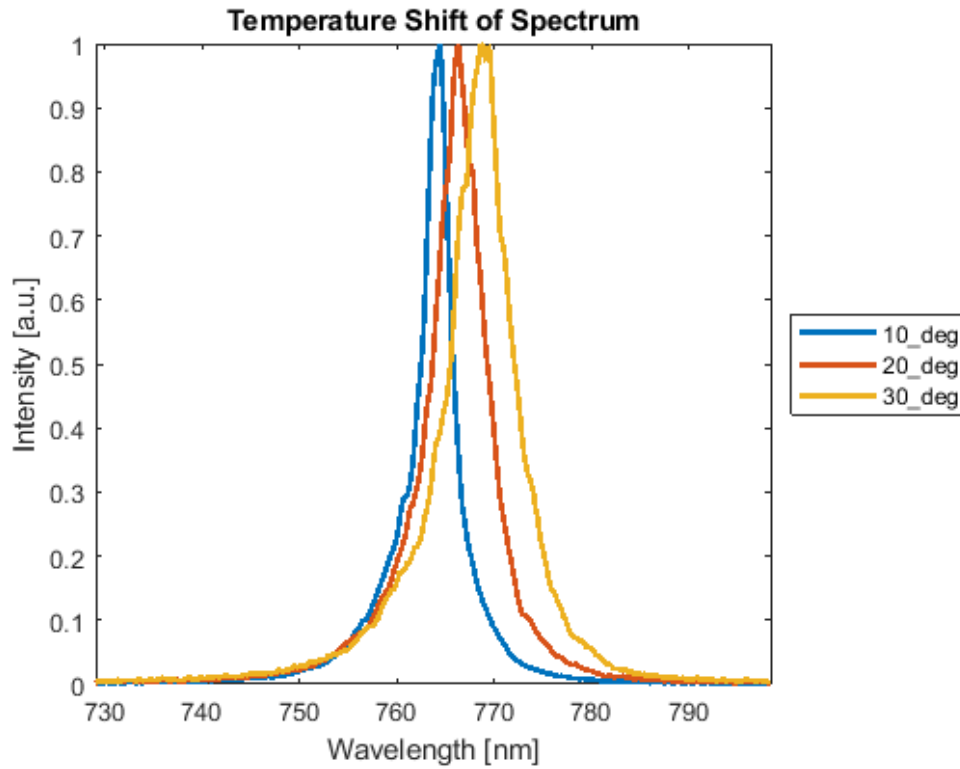


Figure 4.5. This plot depicts the shift in wavelength as the ambient temperature is varied. Ambient temperature was set at 10, 20 and 30 degrees Celsius.

4.7.2 Heat generation calculation

In the quantum well region of the semiconductor laser, heat is generated. The change in temperature in the active region can create changes in refractive index through the Kramers-Kronig relation (discussed in section 3.5.2). Heat generation can be found by using equation:

$$\Delta T = P_D Z_T$$

This uses the power dissipated in the laser (P_D) and the thermal impedance of the material (Z_T) (13). Figure 4.6 shows the calculated values for each device. Broad area diodes can be modelled for heat flow as a one-dimensional flow to the heat sink when the source is relatively close to the heat sink. In this case, the heat sink is the copper tungsten mount. Thermal impedance was found using the following equation, where h is the distance from the quantum well to the heat sink, A is the area of the active region and ξ is thermal conductivity:

$$Z_T = \frac{h}{A\xi}$$

The value of thermal conductivity (ξ) used was approximately 0.45 W/ (cm C) (13). This value was chosen because the wafer substrate is GaAs. The waveguide and cladding layers

between the substrate and quantum well are GaAs-based and relatively small, contributing very little to the thermal conductivity (less than 1%). Higher values of power dissipated indicate lower efficiency in the device, which is shown by a higher change in temperature in the active region of the device as can be seen in Figure 4.6. This also supports the previous reasoning for the use of the double mesa square contact for subsequent analyses.

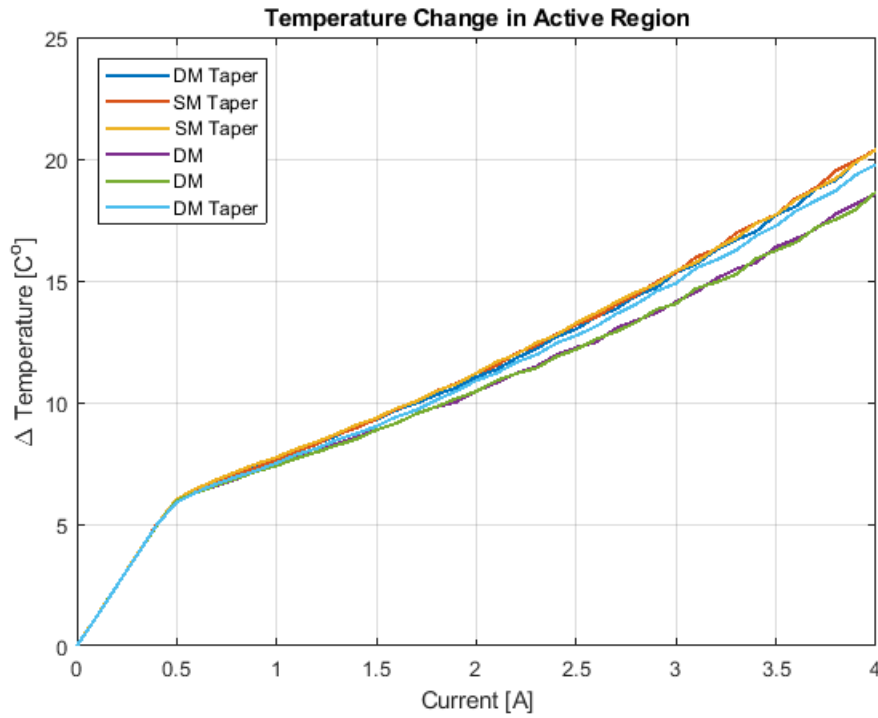


Figure 4.6. The change in temperature in the active region (or generated heat) relative to current was plotted for each device. The double mesa square contact devices have the lowest change in temperature, although the different structures are all still relatively consistent with minimal difference between them.

Using Stern's 1963 work, an estimation of the refractive index change per degree Kelvin is

$$d(\Delta n)/dT \approx 1.6 \times 10^{-4}/^{\circ}K$$

This estimation is valid for temperatures between 100- and 400-degrees Kelvin (27). A change in 20 degrees Celsius corresponds to a change of 20 degrees Kelvin. This leads to a change in refractive index of 0.0032. This estimation constitutes a small portion of what the expected change in refractive index will be during operation. To more accurately calculate the change in refractive index due to temperature, another experiment would need to be conducted where the ambient temperature is changed and the refractive index is calculated using a prism to measure the dispersion angles. This would be done with the material that is used for the fabrication of laser diode, whereas Stern used bulk GaAs for the material.

4.8 Spectral mapping

A custom tool called a Spectral Mapper (diagrammed in Figure 4.7) was developed in order to capture a high-resolution image that depicts wavelength versus position horizontally along the facet of the laser diode. This tool uses a microscope for a base with another optical tool inserted in the optical tube section. This tool uses a diffraction grating to produce a first- or second-order diffraction reflection, allowing for wavelengths to be separated out. By measuring the separation of wavelengths, a thermal gradient along the emitting facet of the laser diode and possible stresses that lead to a change in wavelength can be seen. During the development of this tool, it was seen that it could be used as an alternative to an optical spectrum analyser because it has high enough resolution to spectrally resolve the longitudinal modes.

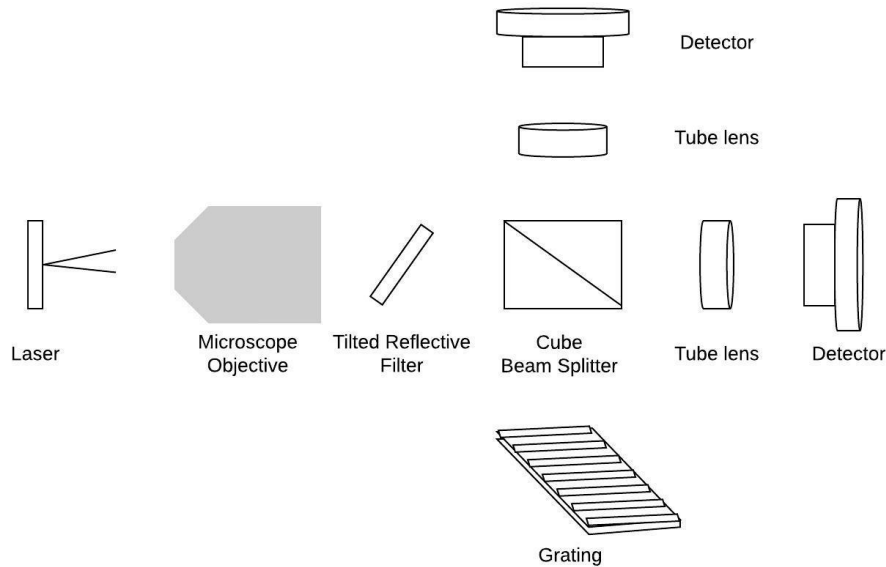


Figure 4.7. This is a diagram of the spectral mapper design. A 50/50 cube beam splitter and 200 mm focal length tube lens were used. The tilted reflective filter was used to prevent external cavities. One detector is used for the spectral mapper image and the other provides a near field image or alignment confirmation.

4.8.1 Tool design

The design of the spectral mapper considers the different variables from the ruled reflective diffraction grating and the focal length of the tube lens. The angle of incidence for the reflective diffraction grating was calculated using this equation:

$$\theta_i = \sin^{-1} \left(\frac{m \times \lambda}{\Delta} \right)$$

where m is the diffraction order, λ is the center wavelength of the incoming light, and Δ is the distance between gratings. The span of wavelengths that could be viewed over the sensor was calculated with equation:

$$\Delta\lambda = \frac{\Delta \times H \times \cos \theta_i}{m \times F}$$

where H is the height of the sensor, and F is the focal length of the tube lens used. These results are shown in Table 4.7.

Grating Order (m):	First-order Reflection			Second-order Reflection		
λ (nm)	θ_i	$\Delta\lambda$	$\Delta\lambda/\text{pixel}$	θ_i	$\Delta\lambda$	$\Delta\lambda/\text{pixel}$
750	26.744	26.588	0.016	64.158	6.489	0.004
760	27.129	26.498	0.016	65.783	6.106	0.004
770	27.516	26.405	0.016	67.518	5.693	0.004
780	27.905	26.312	0.016	69.390	5.240	0.003
790	28.294	26.216	0.016	71.442	4.738	0.003
800	28.685	26.119	0.016	73.740	4.168	0.003

Table 4.7. This table shows the variables affected by wavelength and the grating order reflection where θ_i is the angle of incidence, $\Delta\lambda$ is the change in wavelength and $\Delta\lambda/\text{pixel}$ is the resolution of the device. This gives design parameters and serves as a guide for how to adjust the device for different wavelengths.

4.8.2 Relating the image to the thermal gradient

An analysis of a spectral map image at operating current shows that there is a gradient change in wavelength of 0.224 nm when tracing a single longitudinal mode. By correlating the wavelength change to temperature, a change in temperature of approximately 1 degree Celsius along the facet of the laser diode in the lateral direction is found and therefore a change in refractive index is occurring, indicating a thermal lensing effect. Again, this is using the estimated shift in wavelength due to temperature discussed in section 4.7.1.

Tracing a single longitudinal mode in Figure 4.8, the change in wavelength becomes apparent as it moves through each of the lateral modes where heat would be generated. To further validate these results, this method should be compared to a wavefront sensor scan technique as described by Hall et al. (28) or the technique used by Bawamia et al. where they treated the laser diode as a thick lens (29).

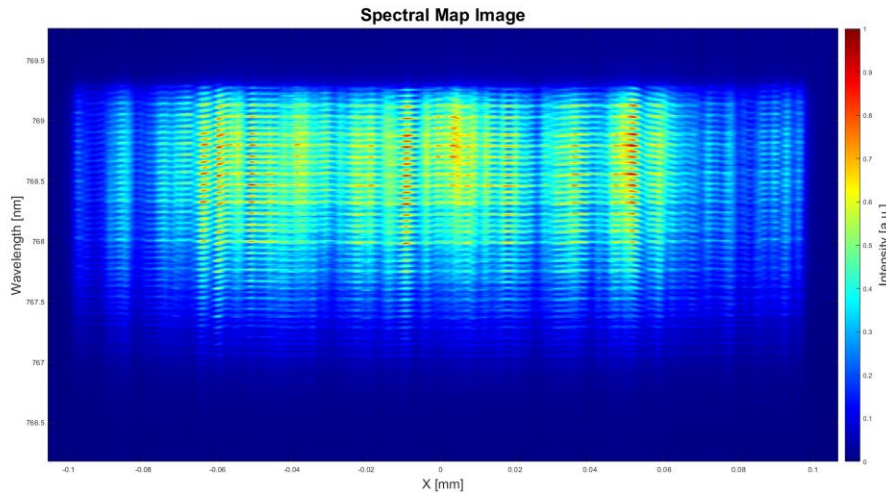
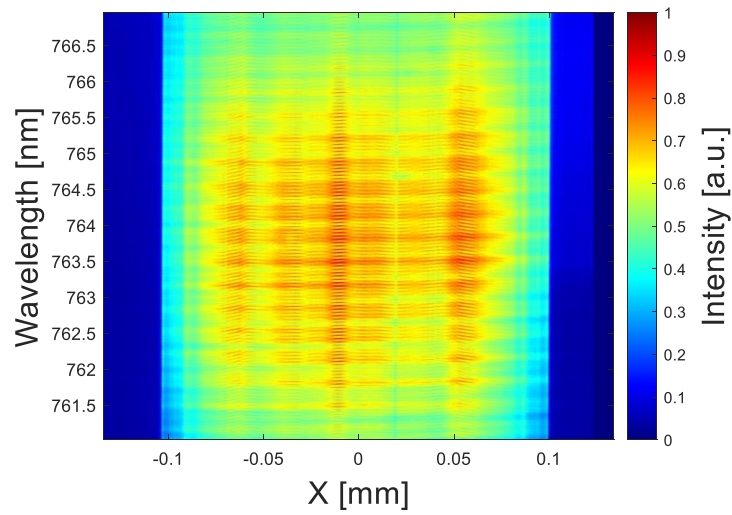


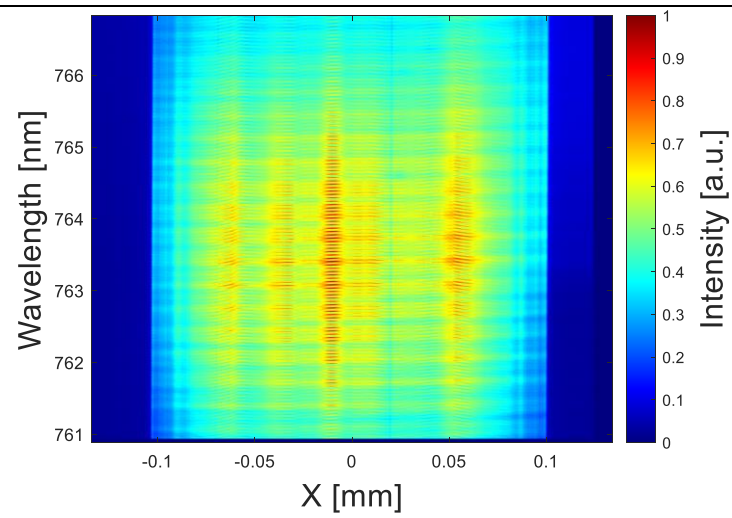
Figure 4.8. This image was taken with the spectral mapper on a double mesa square contact device while the laser current was at 4 Amps and the ambient temperature was at 10 degrees Celsius. It is apparent that a single longitudinal mode shifts between wavelengths as it crosses the lateral modes. The x-axis (X) refers to the position in mm on the front facet of the laser.

4.8.3 Lateral mode progression analysis

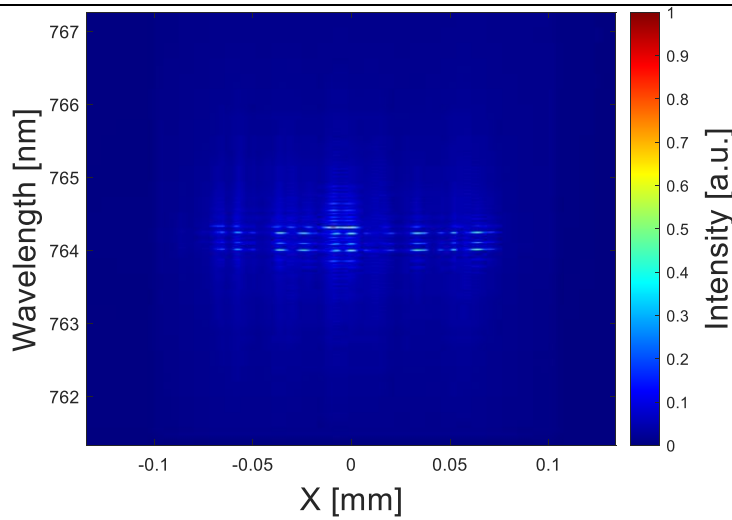
The progression of the lateral modes is apparent as the current is increased (see Figure 4.9). It is apparent that the center wavelength shift from current threshold to 4 Amps is approximately 4.56 nm. Assuming a shift of 0.23 nm per degree Celsius, this matches the calculated temperature rise in the laser above ambient discussed in section 4.7.1. By analysing these images, the number of lateral modes and the width of the lateral modes was found. At threshold current, the number of lateral modes was approximately 18 which progressed to 28 as the current was increased to 4 Amps. The average width of the lateral modes was 4.88 microns at 4 Amps but was difficult to measure at threshold current because the modes were not as developed. Supporting evidence from several sources suggest that individual modes have individual waveguides and can be simplified to a single mode laser (12, 17, 30, 31). Therefore, LaserMOD was used to create a simple cold cavity two-dimensional waveguide structure to model how lateral modes can behave as simple waveguides as suggested by the previous papers. Results of this are discussed in section 5.3.



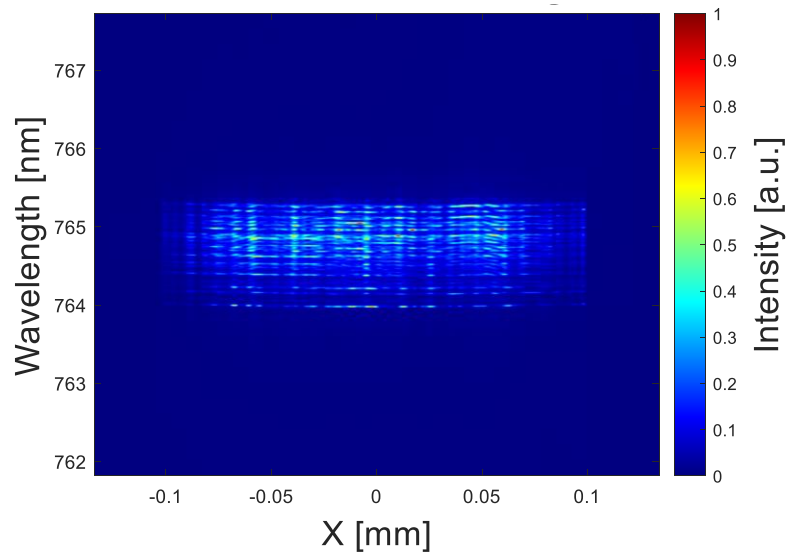
0.473A



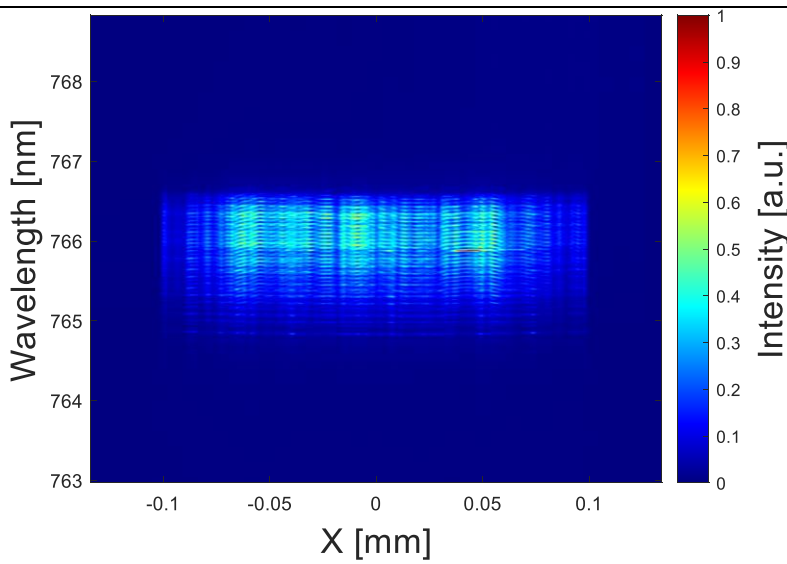
0.5A



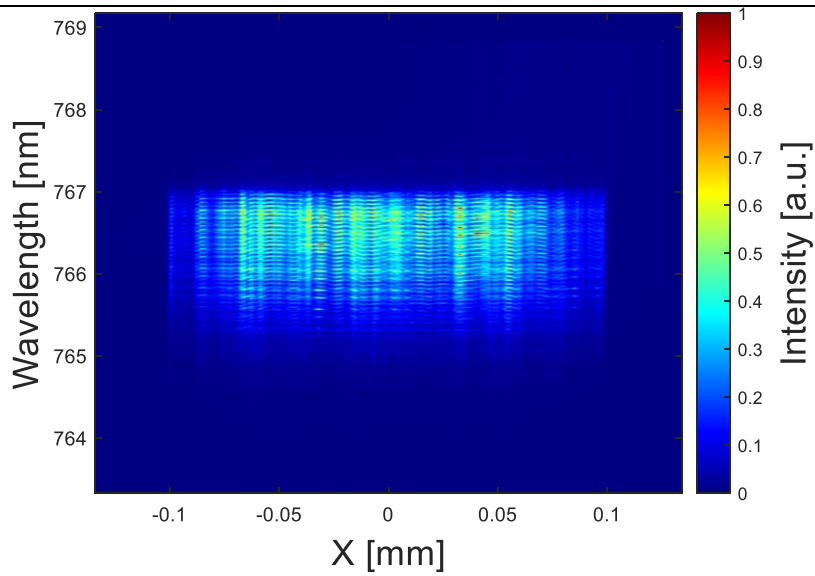
0.545A



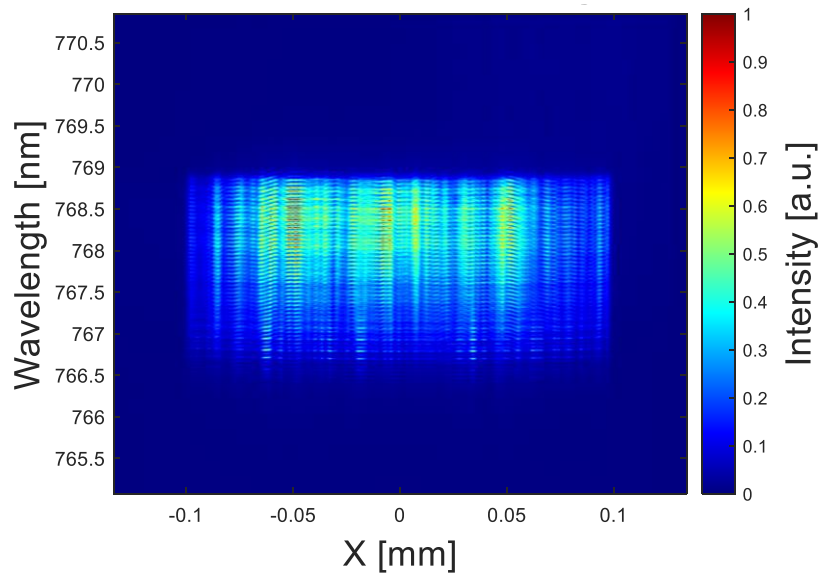
1A



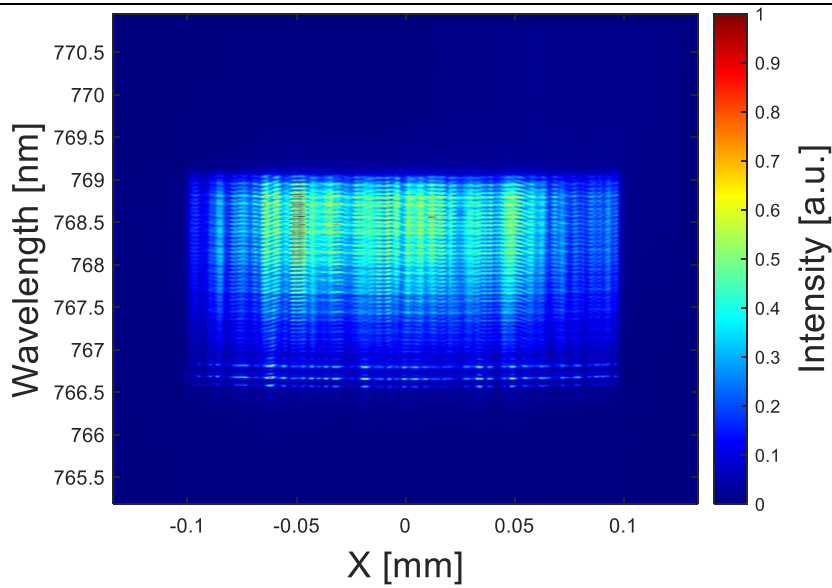
2A



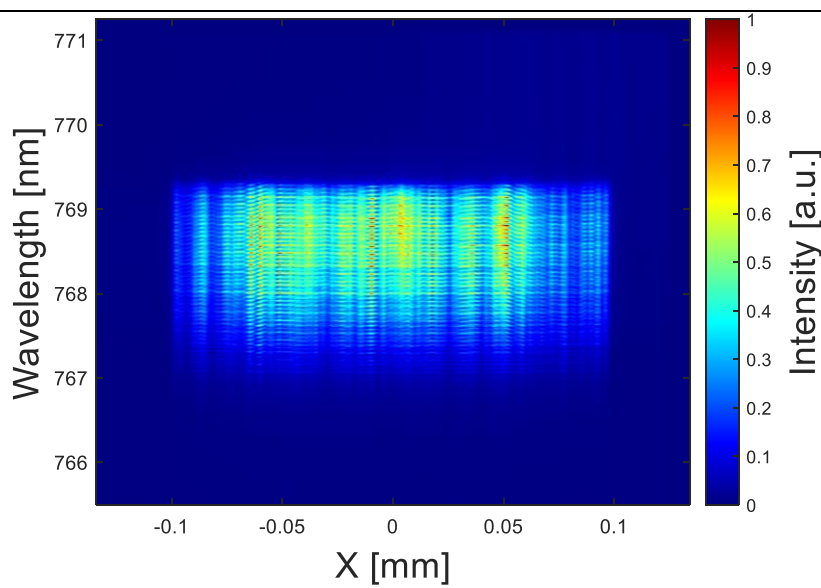
2.28A



3.6A



3.7A



3.9A

Figure 4.9. These images are spectrally resolved images of the laser diode. The progression of these images shows how the lateral and longitudinal modes change as the current is increased. These images also enable the measurement of the width of these modes. The transition from stimulated to spontaneous emission can be seen at low current values where there are few lateral modes. As current increases, high-order lateral modes become apparent.

4.9 Hakki-Paoli test application

4.9.1 Purpose of Hakki-Paoli test

This test was designed to find the gain spectra of a laser diode. It is done by analysing the longitudinal mode modulation while the laser is operating below threshold, generating spontaneous emission (9, 32). It is important to understand the material properties in order to create an accurate model. Because this was the goal of this thesis, this test method was applied to the double mesa laser diodes being characterized.

4.9.2 Applying the Hakki-Paoli method

The Hakki-Paoli test was performed to find the modal gain profile of the laser. Using a high resolution of 0.04 nm, the optical spectrum analyser can find a profile for the intensity versus wavelength. The modal gain profile for a diode laser can be found by measuring the difference between the peaks and valleys of the longitudinal modes. Using equations:

$$\Gamma G_i = \frac{1}{L} \ln \left(\frac{r_i^{1/2} + 1}{r_i^{1/2} - 1} \right) + \frac{1}{L} \ln R$$

$$r_i = \frac{P_i + P_{i+1}}{2V_i}$$

where ΓG_i is the modal gain at threshold, r_i is the depth of modulation, R is the mirror reflectivity (which in this experiment was 3.8% for the anti-reflectivity facet and >95% for the high reflectivity facet), L is the length of the cavity, P is the measured value of a peak, and V is the measured value of a valley. This can be done for each peak and valley corresponding to all wavelengths covered by the emission spectrum (9).

Normally, this is done with diode lasers that have a single mode laterally and transversely. While these various designs are single mode in the transverse direction, they are multi-mode in the lateral direction. This creates the effect of a shorter free spectral range and double peaks in the measured data when using an optical spectrum analyser. Also, reflections in the optical components are a serious consideration, as these can create external cavities having a similar effect as multiple modes. Using the spectral mapper tool provided an alternative to the

optical spectrum analyser. This allowed for the center or dominant lateral mode to be selected and then for the longitudinal modes to be analysed from that region.

4.9.3 Spectral mapper application to Hakki-Paoli

The following figures are the results from applying the spectral mapper discussed in section 4.8 to the Hakki-Paoli test method. Figure 4.10 is the raw image created from the spectral mapper. The next image was created by processing Figure 4.10 with Matlab to find the longitudinal modes in the dominant lateral mode. These data points are graphed in Figure 4.11. The Hakki-Paoli depth of modulation and modal gain calculations were solved using the data points in Figure 4.12 and were plotted in Figures 4.13 and 4.14. This could be challenging because false peaks and valleys could appear in the data and needed to be filtered out in order to obtain accurate depth of modulation values. Using the equation in section 3.4.2, the free spectral range for longitudinal modes was found and it matched the data extracted and plotted in Figure 4.11. Using that free spectral range, a condition was created where peaks and valleys had to be separated by a wavelength of 0.015 nm to be considered valid. If they were not filtered, this would show in the depth of modulation plot because the modulation between the unfiltered points would be very shallow, creating a small depth of modulation value which would appear as holes in the Gaussian shape of the depth of modulation curve. Unfiltered results are shown for comparison in each set of figures. The Matlab codes for this extraction, filtering and calculation are included in the Appendix. The modal gain profile plot showed that the peak gain of the material was at 763.6 nm (Figure 4.14).

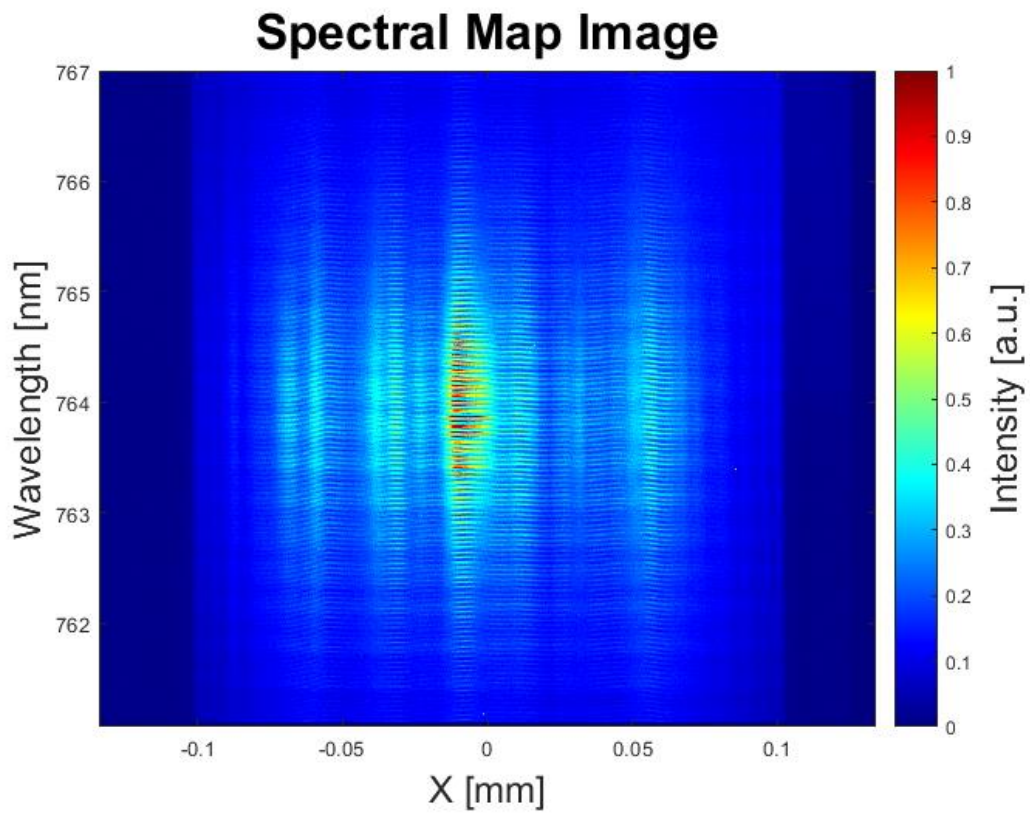


Figure 4.10. This image from the spectral mapper was taken with the laser operating just below threshold current in order to collect data for the calculation of the modal gain.

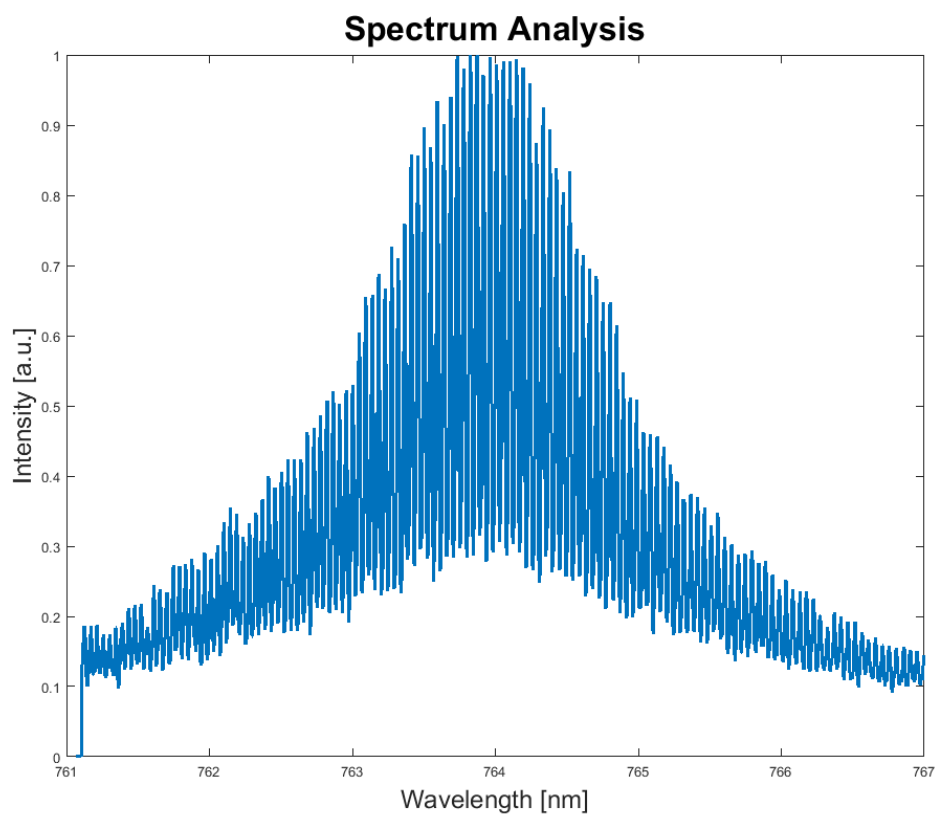


Figure 4.11. The intensity of the dominant lateral mode was plotted to find the longitudinal mode peaks and valleys. These values were extracted using Matlab.

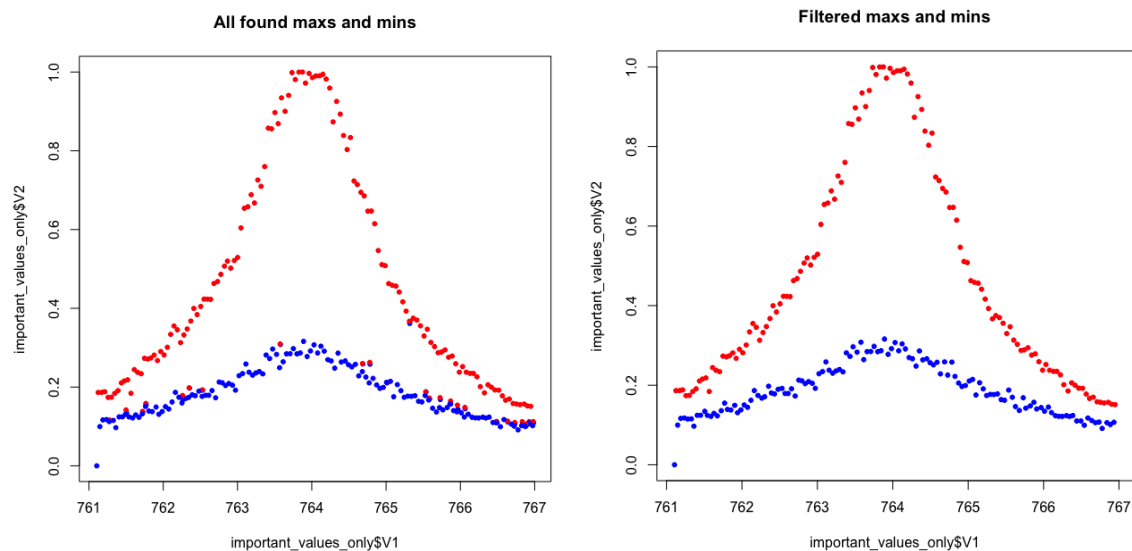


Figure 4.12. These are the extracted peaks and valleys identified in Figure 4.11. The plot on the left shows unfiltered peaks and valleys, where noise created false peaks and valleys. After filtering to peaks and valleys that were at least 0.015 nm apart, true peaks and valleys were correctly identified (see right). These true peaks and valleys were used to calculate the depth of modulation.

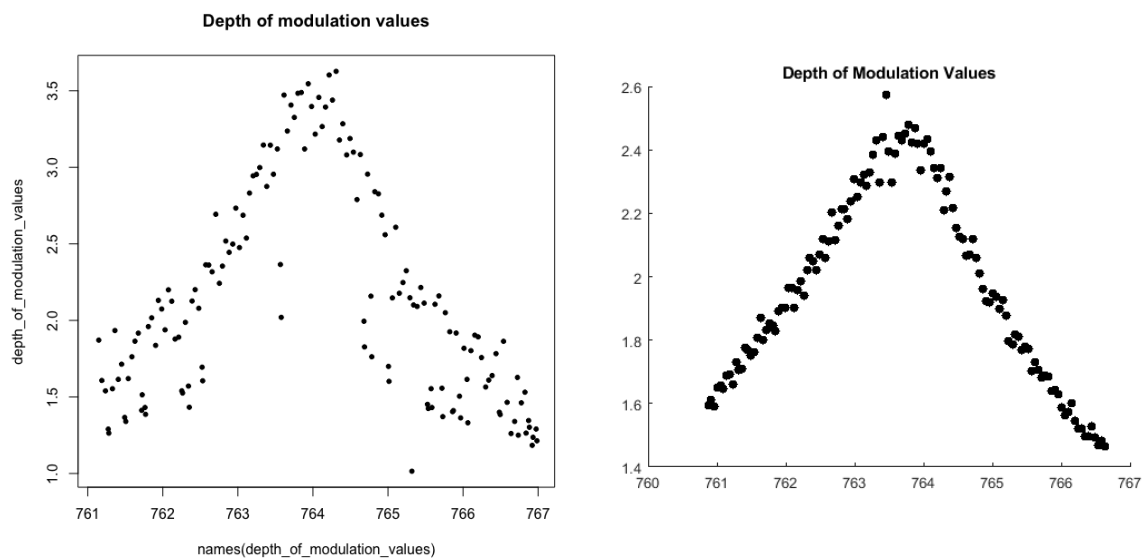


Figure 4.13. Depth of modulation values were plotted. On the left are the values calculated when the unfiltered peaks and valleys are used. The right shows the filtered depth of modulation values. It is apparent that the filtered values produce a cleaner Gaussian curve with less variation and noise, as would be expected.

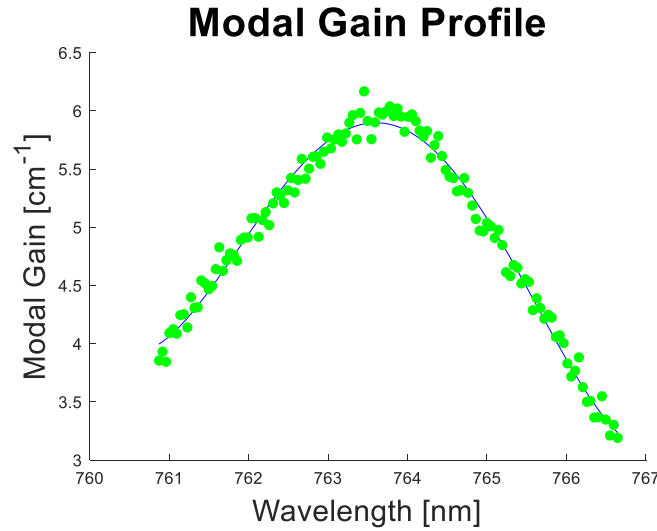


Figure 4.14. These are the plotted values of the modal gain profile for the material, showing that gain is strongest around a wavelength of 763.6 nm.

4.9.4 Internal loss

There are many different methods for calculating internal loss. The first method that was attempted involved testing the properties of the laser at three different cavity lengths. Using the LIV data collected from the three different cavity lengths (0.5 mm, 1.0 mm, 1.5 mm), the following equation was used to calculate internal loss ($\langle \alpha_i \rangle$):

$$\langle \alpha_i \rangle = \frac{n_d - n_d}{Ln_d - L'n_d} \ln \frac{1}{R}$$

where n_d is the differential quantum efficiency, L is the length of the cavity, and R is the mirror reflectivity (13). It is important to note that if the difference in cavity length is not great enough, then the device characteristics, such as central wavelength or output power, will not change as expected with shorter or longer lengths. Because in this experiment, uncoated lasers were cleaved to get the different lengths used and resources did not permit a new photolithography mask to be made to create longer cavity lengths, this method did not provide a useable estimation of internal loss.

Another method to find the internal loss of the device is to use the modal gain at threshold and mirror loss, which is described in the following equation (9):

$$\alpha_m = \frac{1}{2L} \ln(R_1 R_2)$$

The mirror loss can be subtracted from the modal gain at threshold because the modal gain at threshold is when the gain is equal to the loss of the device from mirrors and internal loss.

Internal loss was used in the model to approximate carrier density in a way that mirrored the carrier density of the actual device that was tested. The internal loss was found for the double mesa device (plotted in Figure 4.15).

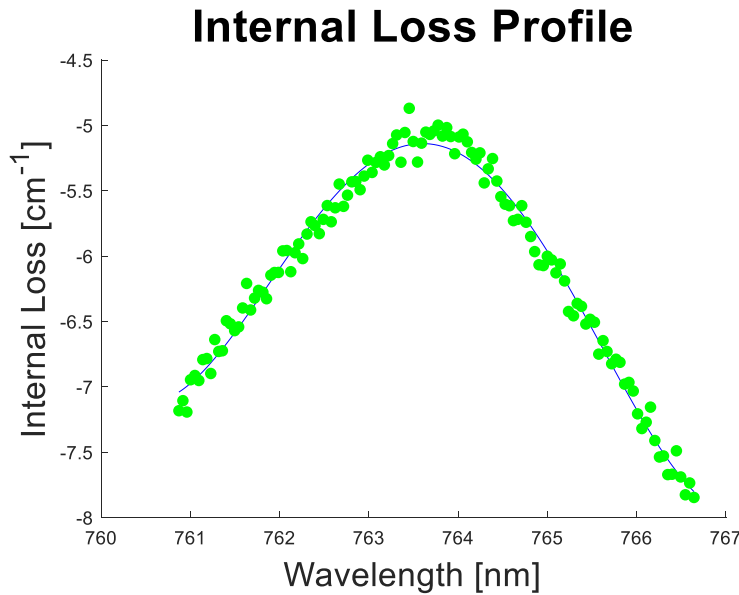


Figure 4.15. This plot shows the values calculated for internal loss. Internal loss is weakest at a wavelength of approximately 763.6 nm. This curve and center wavelength are similar to the modal gain profile because modal gain and internal loss are directly related.

4.10 Phase change to measure refractive index

In this experiment, images were collected with the spectral mapper. Data was extracted using Matlab, which was then plotted and correlated to measurements from a spectrometer.

Changing the temperature altered the wavelength significantly due to the bandgap temperature dependence and was therefore not tested further. By holding the temperature at 10 degree Celsius and varying the applied current, the wavelength shift was monitored.

There are several methods available to calculate the change in refractive index. Using the method described in Crowley et al., the phase change can be related to the refractive index using the following equation:

$$\Delta\phi = \frac{4\pi^2\omega L}{c} \times n$$

where ω is the angular frequency of the bandgap transition, L is the length of the cavity, c is the speed of light in vacuum and n is the refractive index contributions from the effects of interband transitions and intraband excitations of electron and hole populations (10, 33). In order to ensure that the wavelength didn't shift while the laser diode was being operated,

three data points were collected at a single current as shown in Figure 4.16. The oscillations overlap, suggesting no shift in the wavelength under normal operation. Measuring the wavelength from peak to peak of the oscillations, the free spectral range was found to be approximately 0.046 nm. This corresponds to a π phase shift. The current was varied by 1 milliAmp to observe a phase change. Figure 4.17 shows a change of $\pi/2$ phase shift for a 1 milliAmp increase in current and a π phase shift for 2 milliAmps.

The total change in center wavelength from threshold current to 3.8 Amps is 4.56 nm. That change in wavelength would be equivalent to a phase change of 98 π . However, the internal temperature also changes between these current values and, as discussed in section 4.7, the change in temperature would also show a wavelength change that is equivalent to the measured change. Therefore, these results are not conclusive because heating effects changing the bandgap are also causing wavelength shifts, rather than only the effects previously mentioned. In order to overcome this, the laser would have to be pulsed with a narrow pulse width and low duty cycle to keep the laser from generating heat.

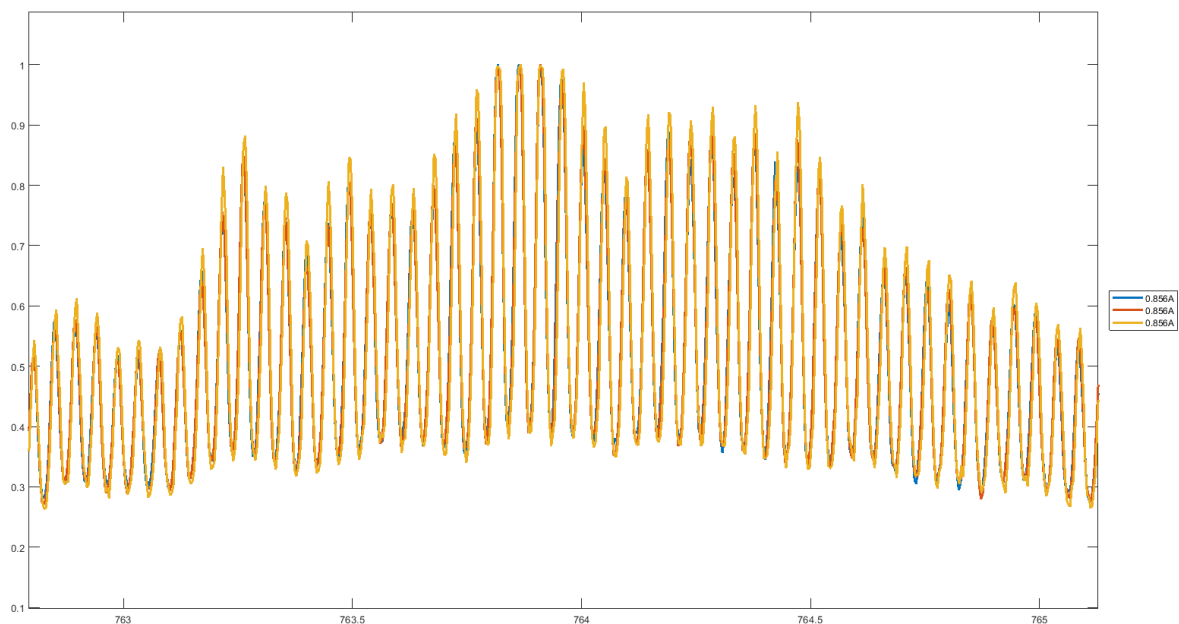


Figure 4.16. As this figure depicts, the normalized spectrum for a single drive current value demonstrates that the spectrum does not shift over time, but is maintained, as shown by the overlapping oscillations. These longitudinal mode oscillations were measured three times for the same device, ambient temperature (10 degrees Celsius) and current (0.856 Amps) to show this consistency. The y-axis is normalized intensity and the x-axis is wavelength in nm.

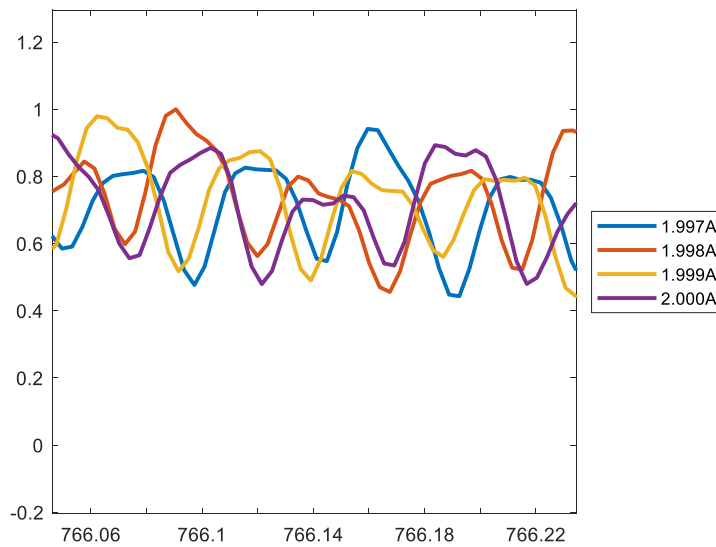


Figure 4.17. This shows the phase change shift with an increase in current of 0.001 Amps. The y-axis is normalized intensity and the x-axis is wavelength in nm.

4.11 Summary

This section included characterization methods for laser diodes and provided the data necessary to build the LaserMOD model and simulations. The spectral mapper overcame the challenge of a many lateral mode laser diode, allowing for the Hakki-Paoli test to be performed to calculate the threshold modal gain and internal loss of the material.

From the LIV testing, it was determined that the input power and output power are directly correlated, and threshold currents are very similar between structures. The tapered contact designs were shown to be less efficient than the square contact. The near-field and far-field characterizations enabled the gathering of data to calculate the lateral beam parameter product. The near field also displayed lateral modal build up in some of the tapered designs, which had the potential to make the beam characteristics of the tapered design worse than the square contact. The intensity profiles and beam divergence values were shown to change as current was increased. The lateral beam parameter product was calculated to assess the different structures. While some structures did have a lateral beam parameter product of a lower value indicating better performance due to a narrower near field, their lateral divergence was still comparable to the other structures. The change in temperature was measured to track the change in center wavelength. This showed that the wavelength shifted by 0.23 nm/degree Celsius. Additionally, non-radiative effects were quantified as the power

dissipated in the laser and input into equations to find the internal heat generated. This internal heat contributed to the change in gain, which through the Kramer-Kronig relation is related to the change in refractive index.

A novel device called a spectral mapper was built that could separate longitudinal modes and track the evolution of lateral modes through increased current. This design was used to gather intensity data from the dominant lateral mode to be used in calculating the gain and internal loss using the Hakki-Paoli test. These values were approximated and used as foundational parameters in the modelling software and simulations in further analyses. The widths of the lateral modes were measured, and the number of lateral modes were tallied as current increased. At higher currents, some of the modes would appear to merge, creating a small multimode area. Phase change analysis was used in an attempt to track the changes in phase of the longitudinal mode as current was increased; however, because we were unable to separate thermal effects from carrier induced effect, the results were not conclusive.

5 Modelling of known structure

5.1 Introduction

This chapter discusses how the LaserMOD modelling software was used in conjunction with the testing and characterization results to gain further insights into the causes of lateral beam divergence. The effects of multiple modes in the waveguide was also assessed as more modes would increase the lateral divergence. Changes in refractive index were simulated with the modelling software to assess the influence on the beam characteristics for comparison with the actual laser diode devices.

5.2 Creating the model from structure details

To begin building the model, the vertical layers of the waveguide are built in the graphical user interface to match the known refractive indices of the device. Shown in Figure 5.1, the vertical refractive index structure can be seen where the quantum well region has a refractive index of approximately 3.6 and is sandwiched between waveguide layers to help confine the mode vertically, both of which are encompassed by cladding layers on the top and bottom. The other layers farther up are from the ridge. These will affect the effective refractive index. These layers were all input into LaserMOD to effectively model the vertical structure.

Because of the unique properties of the quantum well in the actual devices, LaserMOD had difficulties accurately reproducing results that were in agreement with the test data. This led to difficulties creating a model with an equivalent amount of lateral modes in the simulations. At first, an active region with a width of approximately 200 microns was used for the two-dimensional cold cavity simulations; however, the beam divergence was less than +/- 1 degree. Because this was unrealistic, core width variations and refractive index change variations were made to match the cold cavity simulation to the divergence angles of the actual device.

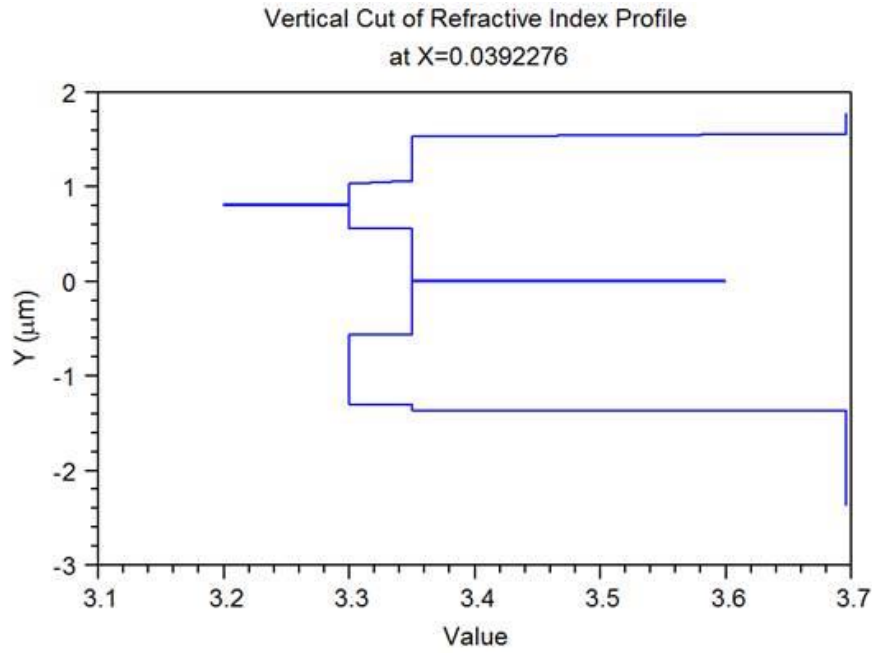


Figure 5.1. This plot shows the vertical refractive index profile of the structure taken at 0.0392276 μm from the center of the device which was used to create the model. The x-axis is the refractive index value and y is the vertical distance in micrometers.

5.3 Results from core width variation with increased modes

By creating a cold cavity two-dimensional lateral waveguide where the index of refraction changed by 0.3 to create confinement, a series of simulations was executed. Material parameters were set to the same as the actual devices. Results are shown in Table 5.1 and Figure 5.2. In Figure 5.2, it is apparent that as the core width increases, the divergence angle decreases exponentially. Interestingly, the more modes in a space, the wider the divergence. The divergence of the slow-axis full width half max can be successfully simulated when looking at a small number of modes and the total divergence can be determined by looking at modes individually. The widths of these modes can be summed to match the core width of the actual device, thereby modelling the number of modes that are present in the actual device. By comparing these widths, we can determine how much of the divergence is due to the modal waveguiding effects (6, 18). The width of the measured modes is similar to the width of the simulated modes for approximately 10 degrees full width half max divergence in the slow axis. While larger than expected changes in refractive index were used that would not realistically be created by carrier-induced effects, this was necessary to attempt to account for thermal effects. Thermal effects would not create these large changes in refractive index;

however, they can create a lensing effect for the modes that would increase the divergence. Therefore, to match the increase in divergence that would be seen with thermal effects, a larger change in refractive index was used in the simulations.

Core Width (μm)	SA FWHM (Deg)			
	1 mode	2 modes	3 modes	4 modes
2	23.6	-	-	-
4	14.2	25	-	-
6	9.4	16.4	18.8	-
8	7	13	15.6	20.65
10	5.7	10.8	12.54	15.6
12	4.8	8.8	10.68	14
14	4	7.54	9.12	12.12
16	3.56	6.6	7.94	11.04
18	3.2	5.9	7.1	9.88
20	2.9	5.3	6.4	8.8
22	2.6	4.8	5.8	8
24	2.4	4.4	5.32	7.4
26	2.2	4	4.9	6.8
28	2	3.7	4.57	6.3
30	1.92	3.5	4.14	5.8

Table 5.1. This table contains the data collected from modelling the far field slow axis full width half max (SA FWHM) divergence. The core width was varied, along with the number of modes being supported, to show how the slow axis changes. A fast axis full width half max divergence of 40 degrees was maintained throughout all simulations. For comparison, the average far field slow axis full width half max divergence for the actual double mesa devices at 4 Amps was 11.35 degrees.

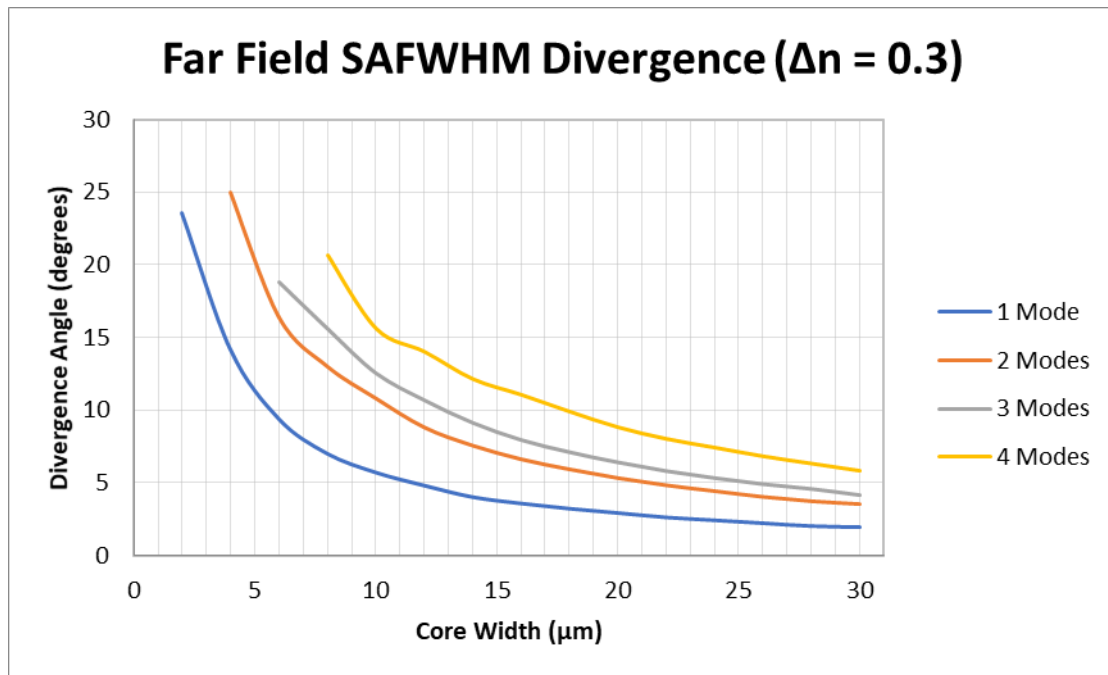


Figure 5.2. This plot shows how divergence angle decreases as the width of the modal waveguide increases. As the number of modes being supported in the core region increases, the divergence angle increases when compared to lower mode numbers, allowing for a wider core region. These values were taken from cold cavity simulations in LaserMOD. The edges of the modal waveguide are created with a change in refractive index (Δn) of 0.3. For comparison, the average far field slow axis full width half max divergence for the actual double mesa devices at 4 Amps was 11.35 degrees.

The simulation software would also support a single mode with the width of the lateral waveguide being changed and a change of refractive index of 0.25 as shown in Figure 5.3. Multiple modes could not be supported with a refractive index change of 0.25 because the confinement was not great enough and modes were leaky, hence why 0.3 was used for multiple mode simulations. It is unclear if there is a limitation in the modelling software or if other factors contributed to the peak in the lower core width simulations. However, it is clear that because the software shows that a mode cannot be supported in that structure without a lateral waveguide with a refractive index change of 0.25 or greater, thermal effects and carrier-induced effects play a large role in the divergence observed in the actual device. Additionally, a two-dimensional model does not account for thermal lensing effects. A three-dimensional model would be needed to appropriately simulate those effects. Not being able to simulate these effects simultaneously makes simulating realistic divergence difficult or impossible when using more realistic values of change in refractive index and thermal lensing.

Core Width (μm)	SAFWHM
2	6.47
4	8.2
6	7.26
8	5.83
10	5
12	4.33
14	3.8
16	3.32
18	3
20	2.74
22	2.5
24	2.3
26	2.15
28	2
30	1.88

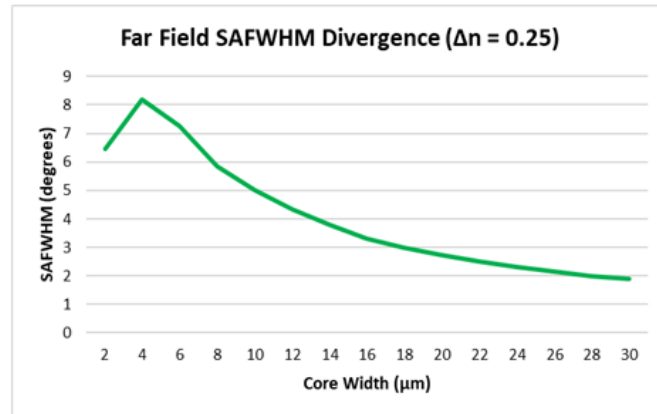


Figure 5.3. This plot shows how divergence angle (slow axis full width half max angle) decreases as the width of the modal waveguide increases for a single mode. These values were taken from cold cavity simulations in LaserMOD. The edges of the modal waveguide are created with a change in refractive index (Δn) of 0.25. More than a single mode could not be supported in the modal waveguide with that small of a refractive index change due to weak confinement and leaky modes. For comparison, the average far field slow axis full width half max divergence for the actual double mesa devices at 4 Amps was 11.35 degrees.

For the fast-axis divergence, changes in the lateral width did not have any effect; therefore, changes in the vertical refractive index were investigated to find causes for the change in fast-axis divergence. The fast-axis full width half max (FAFWHM) divergence was measured from the simulations and plotted in Figure 5.4. This shows how a change in the vertical refractive index in the waveguide and cladding layers would change the confinement of the mode vertically, resulting in a change in the fast-axis divergence.

Δn	FAFWHM
0	34
0.01	34.86
0.02	35.5
0.03	36.5
0.05	37.11
0.1	39
0.2	40.2

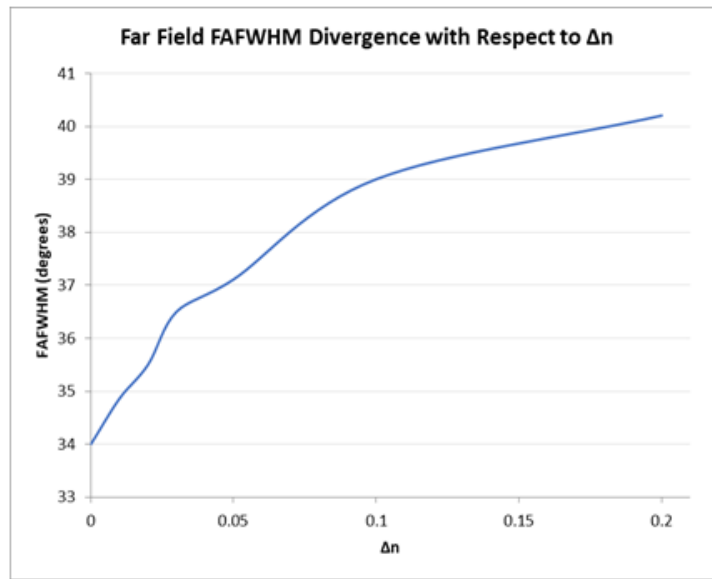


Figure 5.4. This plot shows how divergence angle (fast axis full width half max angle) increase as the change in refractive index increases. These values were taken from cold cavity simulations in LaserMOD. For comparison, the average far field fast axis full width half max divergence for the actual double mesa devices at 4 Amps was 37.50 degrees.

5.4 Using LaserMOD to find refractive index changes

Using a full model of the laser structure, the change in refractive index due to carrier-induced effects was simulated. Figure 5.5 shows how the refractive index is changed with different carrier densities with the properties of the laser diode materials input into LaserMOD. The results are suspicious because the refractive index change is lower than expected. According to Bennett et al, a change of approximately 0.1 would be reasonable for a laser diode of this material (8). Another reason the results are suspicious is because the only significant positive refractive index change comes from the lateral temperature profile, the bandgap shrinkage and the stresses in the active region and negative changes come from the free carrier absorption and band-filling. Given that for this structure the index change is not as large as the expected change approximated by Bennett et al., a larger net change in refractive index would be expected than what is shown in Figure 5.5. This is because LaserMOD simulations do not account for the thermal effects or the stresses induced by packaging.

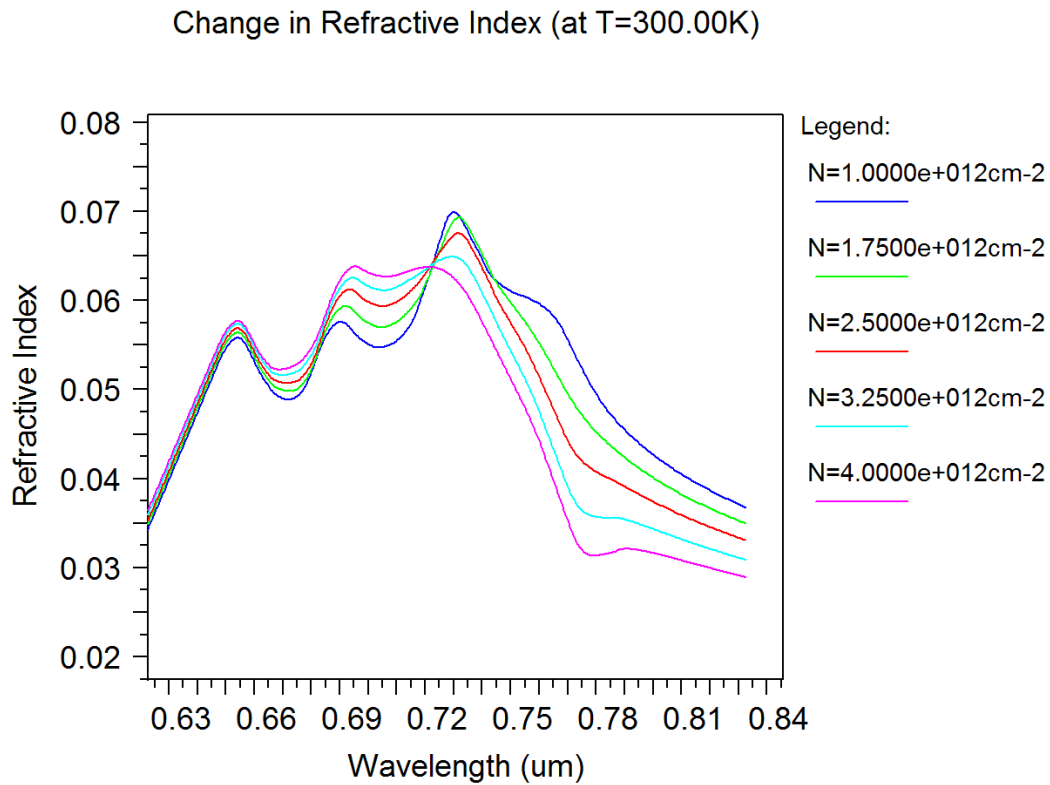


Figure 5.5. LaserMOD simulated change in refractive index due to carrier-induced transitions as a function of real carrier density for laser material operating at 0.78 μm .

5.5 Summary

Due to the complexities of the laser diode structure, LaserMOD had difficulties accurately simulating all the different contributing variables. Because of this, the simple waveguide model approach was taken to gain insight into how the modal density would affect the divergence, as discussed in section 4.3. The variations of core width and lateral change of refractive index were made in an attempt to understand how carrier-induced and thermal effects would affect the laser diode. Some insight was gained into the expected change in refractive index due to carrier-induced effects. LaserMOD was not able to include thermal effects in the simulations because the simulations use a two-dimensional model; a three-dimensional model would be needed to accurately simulate these effects. While these simulations and experiments did not cover all the effects previously discussed in section 2, they did illustrate that without thermal effects, a change of refractive index of approximately 0.25 would be needed to support the modes and model the divergence seen in the actual devices. This indicates that thermal effects play a much stronger role in the device and are able to overcome the carrier-induced effects to

create the observed divergence. Importantly, it also shows how in the simple waveguides, the individual modes can affect the divergence of the laser. A full model of near field and far field is beyond the scope of this thesis. Here we seek to construct a simple model to reproduce the main trends observed in the characterization of the laser diodes.

Preliminary full model results are included in appendix 7.2. All figures are from a two-dimensional cross-sectional isothermal simulation.

6 Summary

6.1 Achievements

The major achievements and take-away points from each portion of the thesis are detailed below. While each section had different types of outcomes, they both contribute to the ability to characterize and begin to improve the understanding of lateral divergence in semiconductor laser diodes.

6.1.1 Testing and characterization

- LIV testing revealed that input and output power are directly correlated, and that threshold currents are very similar between structures. The tapered contact designs were shown to be less efficient.
- Near field characterization found the beam waist for different devices and provided insight into the intensity profile at the front facet of the laser. The tapered devices commonly showed modal build-up at the edges of the active region.
- The far field characterization yielded beam divergence values and demonstrated how the divergence evolves through increased current.
- The lateral beam parameter product showed how near and far field can be combined and was used in the building of the model. This metric is also used as metric for fiber coupling and is therefore an important aspect of laser diode characterization. Additionally, the tapered contact devices with modal build-up were shown to have poorer beam characteristics. If efficiency and modal build-up could be consistently overcome, the tapered contact devices would be advantageous compared to the square contact devices.
- The analysis of temperature effects revealed how non-radiative effects create heat in the active region of the laser. The tapered contact devices showed larger amounts of heat generated in the active region, supporting the previous observation of poorer efficiency when compared to the square contact devices.
- A novel tool called a spectral mapper was developed that could be used to separate longitudinal modes and display the evolution of the lateral modes through increased current. This enabled the collection of longitudinal mode intensity values for input into subsequent analyses, as well as the measurement of modal width and accurate counting of modes present at specific currents.

- The Hakki-Paoli test calculated the threshold modal gain and internal loss from measured data. It was determined that an optical spectrum analyser does not work with a lateral multimode device; however, by using the spectral mapping technique, the dominant lateral mode could be analysed to approximate the values of the material.

6.1.2 Modelling and simulations

- A model was created that included all successfully measured results from actual structures. Phase change results were excluded, which were ambiguous due to inability to separate temperature and carrier-induced effects.
- Cold cavity two-dimensional models were simulated to accurately represent modal waveguides and assess the divergence created by individual modes. By varying the core width with increasing numbers of modes, it was determined that more modes inside the waveguide increased the amount of divergence.
- It was determined that the model was limited to the amount of modes it could support inside of a waveguide due to weak confinement.
- Using modelling software, the refractive index change in the material was estimated due to carrier effects. It was determined that modelling software has limitations where it underestimates the change in refractive index because it cannot incorporate thermal effects and carrier-induced effects simultaneously.

6.2 Future Work

In order to more accurately approximate the total change in refractive index, the device should be pulsed with a narrow pulse width and low duty cycle to remove thermal effects. This would allow for thermal effects to be separated from carrier effects so their contributions could be accounted for in the total effect. Also, to verify the thermal lensing measurement with the spectral mapper, a high-resolution wave front sensor scan method should be performed (28, 29). All of the characterization and testing could be done using a polarization filter to separate the transverse magnetic and transverse electric light. This would account for stresses induced into the material during the packaging process or at other times during the fabrication.

Ultimately, this work could be applied to high-power diode lasers particularly in coupling efficiency research or beam shaping of high-power lasers because this is helping to

understand the root causes of divergence. This would enable any important factors to be addressed as early as the design phase, rather than being addressed, as they currently are, during the assembling of the coupling or beam shaping optics.

7 Appendix

7.1 Matlab script for Hakki-Paoli method

```
%% Import Data
close all
clear all
clc

dpath = '\\Tusfile02\Development\Optical_Design\NickV\SM_Test\';

% Import Image

[ipath,dipath] = uigetfile('*', 'Select Image');
ipath = [dipath, ipath];

[spath, dspath] = uigetfile('*', 'Select Spectral Data');
spath = [dspath, spath];

%I = double(rgb2gray(importdata(ipath))); %Color image/mono16
I = double(importdata(ipath)); %Gray Image
I = rot90(I,-1); %rot90(I,1); % maybe

Sraw = importdata(spath);
Sraw = Sraw.Sheet1;
S.x = Sraw(:,1)';
S.y = Sraw(:,2)';

%% Calculations

% Center I
[N,M] = meshgrid(1:size(I,2),1:size(I,1));
[cm,cn] = centroid(I);
Icent = interp2(N-(cn-size(I,2)/2),M-(cm-size(I,1)/2),I,N,M);
Icent(isnan(Icent)) = 0;
%I = Icent./max(Icent(:));
I = normalize(Icent); %2019 Broke this

mag = 20; % system magnification

threshS = 0.2;
Sytemp = normalize(S.y);
Sytemp(Sytemp < threshS) = 0;
centSidx = centroid(Sytemp);
centSwl = interp1(1:length(Sytemp),S.x,centSidx).*1e-9;

threshI = 0.2;
Iytemp = normalize(sum(I,2));
Iytemp(Iytemp < threshI) = 0;
centIidx = centroid(Iytemp);

g_p=1200000; % lines/m
mmpx = 4.4615e-3; % Double check...
m=2;
% centSwl=769e-9; %m
F=0.200; %m
pixel_count=size(I,1);
```



```

theta=asin((m*centSwl)/(2/g_p));
lit_angle=rad2deg(theta);
H_sensor=mmpx.*1e-3*pixel_count;
dlam=(H_sensor/g_p*cos(theta))./(m*F)*1e9;
pixelscalefactor=dlam/pixel_count;

WL_scale=(1:pixel_count).*pixelscalefactor-dlam/2; % 1-nm offset on station map

centIwloffset = interp1(1:length(WL_scale),WL_scale,centIidx).*1e-9;

WL_scale=WL_scale*-1+centSwl.*1e9+centIwloffset.*1e9; % either + or -

x_scale = linspace(-size(I,2)*mmpx/2,size(I,2)*mmpx/2,size(I,2))./mag;

%nrng = 680:690; %Estimated range for the fine step images

nrng = 551:567;%for 0.530A

% figure
% imagesc(I)
% colormap(jet)
% axis image
% w = ginput(2); % Start left find range of values to sum over
% nrng = round(w(:,1));

%yI = sum(I,2); % Ysum
yI = sum(I(:,nrng),2); % Ysum
%yI = I(:,round(end/2-40)); %Single Slice T120ED

%% Figures

figure
imagesc(x_scale,WL_scale,I)
%colormap(jet(1e3))
%axis xy
xlabel('X [mm]','fontsize',18)
ylabel('Wavelength [nm]','fontsize',18)
axis xy
title('Spectral Map Image','fontsize',24)
colormap(jet(1e3))
zrng = [0,1];
caxis(zrng)
cb = colorbar;
ylabel(cb,'Intensity [a.u.]','fontsize',18)

figure
% plot(S.x,normalize(S.y),'linewidth',2)
% hold on
plot(WL_scale,normalize(yI),'linewidth',2)
title('Spectrum Analysis','fontsize',24)
xlabel('Wavelength [nm]','fontsize',18)
ylabel('Intensity [a.u.]','fontsize',18)
%% Depth of Modulation section

%% Calculate the depth of modulation by identifying min and max points from image data

% User specified expected distance from min to max
expected_min2max_distance = 0.02;

yIN = normalize(yI);

```

```

WL_scale = WL_scale';
wvlength_plot1 = [WL_scale yIN];
wvlength_plot = array2table(wvlength_plot1, 'VariableNames',{ 'Wavelength','Value'});

max_array = [];
min_array = [];
%%%%%%%%%%%% Get max and min values
% Skip first and last values since can't be min or max.
for i = 2:(size(wvlength_plot,1) - 1)
    value_i = wvlength_plot.Value(i);

    prev_value = wvlength_plot.Value(i-1);
    next_value = wvlength_plot.Value(i+1);

    wvlength_i = wvlength_plot.Wavelength(i);

    if (value_i > prev_value) && (value_i >= next_value)
        max_array((size(max_array,1) + 1),1:2) = [wvlength_plot.Wavelength(i) value_i];
    elseif (value_i < prev_value) && (value_i <= next_value)
        min_array((size(max_array,1) + 1),1:2) = [wvlength_plot.Wavelength(i) value_i];
    else
        continue;
    end
end

% Add designation to data points
wvlength_plot.Extrema = string(zeros(size(wvlength_plot,1), 1));
for i = 1:size(wvlength_plot,1)
    if ismember(wvlength_plot.Wavelength(i), max_array(:,1))
        wvlength_plot.Extrema(i) = "Max";
    elseif ismember(wvlength_plot.Wavelength(i), min_array(:,1))
        wvlength_plot.Extrema(i) = "Min";
    end
end

% Pull out maxs and mins
wvlength_plot.Extrema = categorical(wvlength_plot.Extrema);
important_values_only = wvlength_plot((wvlength_plot.Extrema == "Max" | wvlength_plot.Extrema ==
"Min"),:);

colors_designations = important_values_only.Extrema;
colors_designations(colors_designations == "Min") = 'blue';
colors_designations(colors_designations == "Max") = 'red';
figure
scatter(important_values_only.Wavelength, important_values_only.Value, [], colors_designations, 'filled');
title('All Extrema')

%%%%%%%%%%%% Remove side-by-side maxs and mins
important_values_only = remove_adjacent_extrema(important_values_only);

%%%%%%%%%%%% Remove maxs and mins that are too close to one another
important_values_only = important_values_only((important_values_only.Distance >
(expected_min2max_distance/2)),:);

% Make sure filtering by distance didn't cause adjacent extrema
if (size(unique(important_values_only.Extrema(1:2:size(important_values_only,1)))) ~= 1) |
(size(unique(important_values_only.Extrema(2:2:size(important_values_only,1)))) ~= 1)
    disp("Distance-based removal didn't work as expected. Re-removed side-by-side maxs and mins. May need
double checking.")

```

```

important_values_only = remove_adjacent_extrema(important_values_only);
end

colors_designations = important_values_only.Extrema;
colors_designations(colors_designations == "Min") = 'b';
colors_designations(colors_designations == "Max") = 'r';
figure
scatter(important_values_only.Wavelength, important_values_only.Value, [], colors_designations, 'filled');
title('Filtered Extrema')

%writetable(important_values_only,'C:/Users/catch/Desktop/filtered_maxs_and_mins.txt','Delimiter','\t','WriteR
owNames',false);

%%%%%%%%%% Calculate depth of modulation
min_array = important_values_only((important_values_only.Extrema == "Min"),{'Wavelength', 'Value'});
max_array = important_values_only((important_values_only.Extrema == "Max"),{'Wavelength', 'Value'});

depth_of_modulation_values = [];
if important_values_only.Extrema(1) == "Min"
    for i = 2:size(min_array, 1)
        depth_value = (max_array.Value(i-1) + max_array.Value(i))/(2 * min_array.Value(i));

        depth_of_modulation_values((i-1), 1:2) = [min_array.Wavelength(i), depth_value];
    end
else
    for i = 1:(size(min_array, 1)-1)%changed this to max_array from min_array
        depth_value = (max_array.Value(i) + max_array.Value(i+1))/(2 * min_array.Value(i));

        depth_of_modulation_values(i, 1:2) = [min_array.Wavelength(i), depth_value];
    end
end

figure
scatter(depth_of_modulation_values(:,1), depth_of_modulation_values(:,2), [], 'black', 'filled');
title('Depth of Modulation Values')

gain_values = modal_gain_calc(depth_of_modulation_values);

p = polyfit(gain_values(:,1),gain_values(:,3), 4);
pol_gain = polyval(p,gain_values(:,1));

figure
%plot(gain_values(:,1), gain_values(:,3))
hold on
plot(gain_values(:,1), pol_gain,'b-')
scatter(gain_values(:,1), gain_values(:,3),[],'g','filled')
title('Modal Gain Profile','fontsize',24)
xlabel('Wavelength [nm]','fontsize',18)
ylabel('Modal Gain [cm^{-1}]','fontsize',18)

Intloss = int_loss_calc(depth_of_modulation_values);

K = polyfit(Intloss(:,1),Intloss(:,3), 4);
pol_Intloss = polyval(K,Intloss(:,1));

figure

```

```

hold on
plot(Intloss(:,1), pol_Intloss,'b-')
scatter(Intloss(:,1), Intloss(:,3),[],'g','filled')
title('Internal Loss Profile','fontsize',24)
xlabel('Wavelength [nm]','fontsize',18)
ylabel('Internal Loss [cm-1}','fontsize',18)

function y = remove_adjacent_extrema(important_values_table)
    rows_to_remove = [];
    for i = 2:size(important_values_table,1)
        comparison_values = [i i-1];
        %comparison_values

        if important_values_table.Extrema(i) == important_values_table.Extrema(i-1)
            if important_values_table.Extrema(i) == "Max"
                not_max = comparison_values(important_values_table.Value(comparison_values)...
                    ~= max(important_values_table.Value(comparison_values(1)),
important_values_table.Value(comparison_values(2))));
                %not_max
                rows_to_remove(size(rows_to_remove)+1) = not_max;
            elseif important_values_table.Extrema(i) == "Min"
                not_min = comparison_values(important_values_table.Value(comparison_values)...
                    ~= min(important_values_table.Value(comparison_values(1)),
important_values_table.Value(comparison_values(2))));
                %not_min
                rows_to_remove(size(rows_to_remove)+1) = not_min;
            end
        end
    end
    important_values_table(rows_to_remove,:) = [];

    important_values_table.Distance = zeros(size(important_values_table,1), 1);
    for i = 2:size(important_values_table, 1)
        important_values_table.Distance(i) = important_values_table.Wavelength(i-1) -
important_values_table.Wavelength(i);
    end

    y = important_values_table;
end

function y=modal_gain_calc(depth_of_modulation_values)

    L = 2*0.15;
    R = 0.038*0.96;

    for i = 1:size(depth_of_modulation_values,1)
        net_gain = (1/L)*log((sqrt(depth_of_modulation_values(i,2))+1)/...
            (sqrt(depth_of_modulation_values(i,2))-1)) + (1/L)*log(R);

        depth_of_modulation_values(i, 3) = -1*net_gain;
    end

    y = depth_of_modulation_values;
end

function y=int_loss_calc(depth_of_modulation_values)

    L = 2*0.15;
    R = 0.038*0.96;

```

```

for i = 1:size(depth_of_modulation_values,1)
    net_gain = (1/L)*log((sqrt(depth_of_modulation_values(i,2))+1)/...
        (sqrt(depth_of_modulation_values(i,2))-1));% + (1/L)*log(R);

    depth_of_modulation_values(i, 3) = -1*net_gain;
end

y = depth_of_modulation_values;
end

```

7.2 Full model simulation results

These are preliminary results from a full model simulation. The far field fast axis results matched the data tested in actual devices. The slow axis also matched, but the intensity profile had characteristics that were not physically possible in an actual device. Further investigation is needed to determine what caused these effects and to create a more realistic model.

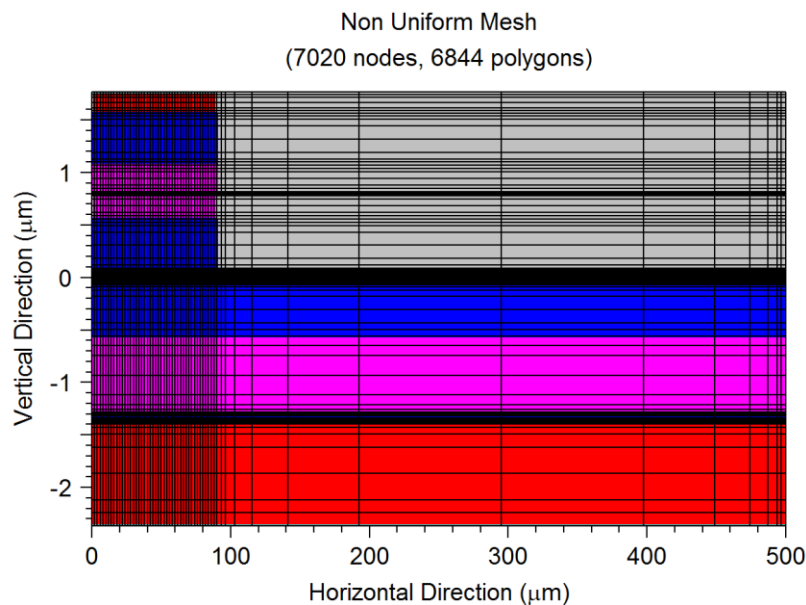


Figure 8.1. LaserMOD simulated symmetrical structure mesh grid for KP Eigen Vector simulation. Used with a two-dimensional isothermal model.

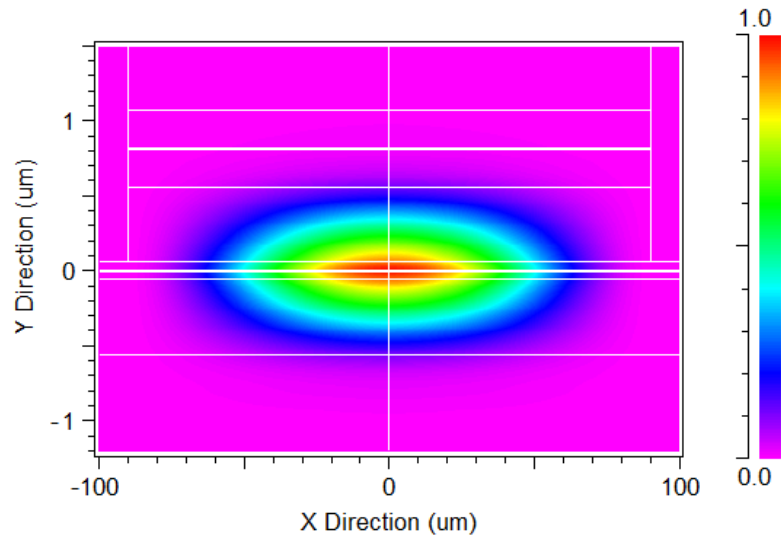


Figure 8.2. LaserMOD simulated primary mode under bias to current threshold.

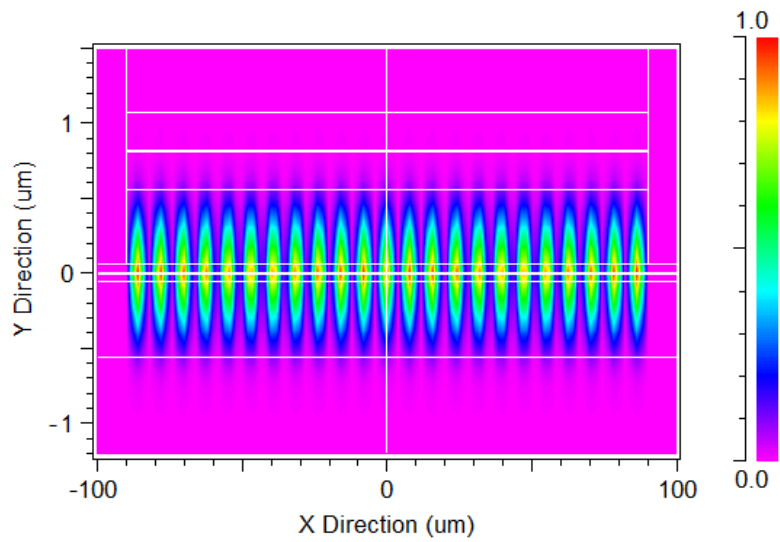


Figure 8.3. LaserMOD simulated higher order mode to show symmetrical modal distribution.

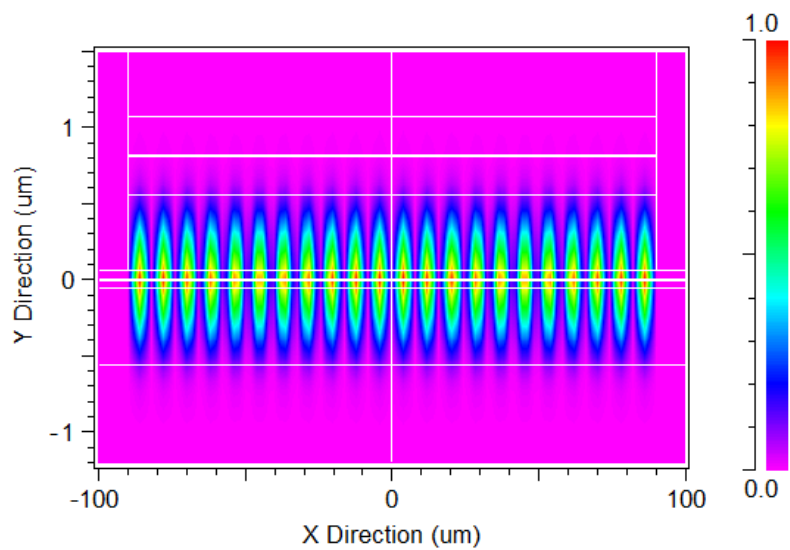


Figure 8.4. LaserMOD simulated higher order mode to show asymmetrical modal distribution.

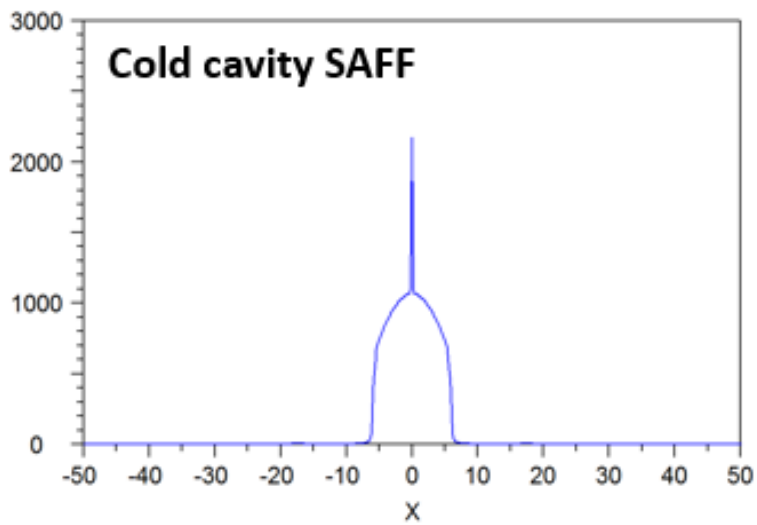


Figure 8.5. LaserMOD simulated cold cavity slow axis far field. Displays unrealistic peak in the center of the distribution. The x-axis is far field (degrees) and the y-axis is intensity.

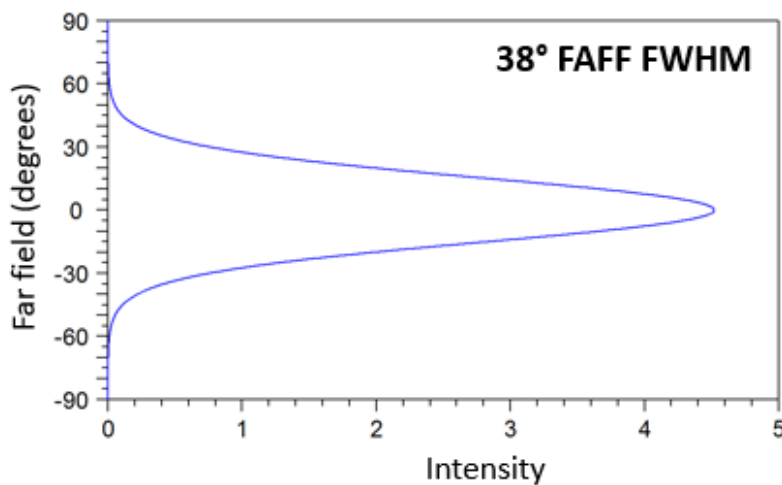


Figure 8.6. LaserMOD simulated fast axis far field with device under bias to current threshold. The fast axis full width half max is consistent with the tested device.

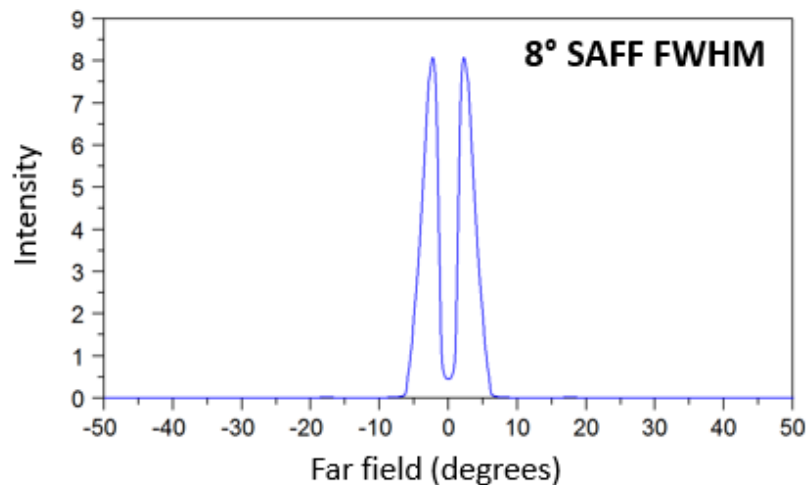


Figure 8.7. LaserMOD simulated slow axis far field with device under bias to current threshold. The slow axis full width half max is consistent with the tested device, but the dip in the center of the intensity profile is not physically possible.

```

mode [0,0]: power = 0.0015 mW
mode [1,0]: power = 0.0017 mW
mode [2,0]: power = 0.0021 mW
mode [3,0]: power = 0.0028 mW
mode [4,0]: power = 0.0040 mW
mode [5,0]: power = 0.0059 mW
mode [6,0]: power = 0.0093 mW
mode [7,0]: power = 0.0167 mW
mode [8,0]: power = 0.0403 mW
mode [9,0]: power = 0.4358 mW
mode [10,0]: power = 2.7675 mW
mode [11,0]: power = 4.6837 mW
mode [12,0]: power = 6.0607 mW
mode [13,0]: power = 7.0285 mW
mode [14,0]: power = 7.6857 mW
mode [15,0]: power = 8.1102 mW
mode [16,0]: power = 8.3621 mW
mode [17,0]: power = 8.4447 mW
mode [18,0]: power = 8.5257 mW
mode [19,0]: power = 8.5197 mW
mode [20,0]: power = 8.4377 mW
mode [21,0]: power = 8.2843 mW
mode [22,0]: power = 8.0884 mW
mode [23,0]: power = 7.7974 mW
mode [24,0]: power = 7.4493 mW
mode [25,0]: power = 7.0560 mW
mode [26,0]: power = 6.5593 mW
mode [27,0]: power = 6.2328 mW
mode [28,0]: power = 5.9030 mW
mode [29,0]: power = 5.5746 mW
mode [30,0]: power = 5.2501 mW
mode [31,0]: power = 4.9151 mW
mode [32,0]: power = 4.5749 mW
mode [33,0]: power = 4.2209 mW
mode [34,0]: power = 3.8325 mW
mode [35,0]: power = 3.5849 mW
mode [36,0]: power = 3.3387 mW
mode [37,0]: power = 3.0969 mW
mode [38,0]: power = 2.8495 mW
mode [39,0]: power = 2.6288 mW
mode [40,0]: power = 2.3778 mW
mode [41,0]: power = 2.3369 mW
mode [42,0]: power = 1.3648 mW
mode [43,0]: power = 1.2281 mW
mode [44,0]: power = 1.2086 mW
mode [45,0]: power = 1.1651 mW
mode [46,0]: power = 1.0214 mW
mode [47,0]: power = 0.0000 mW
mode [48,0]: power = 0.0000 mW
mode [49,0]: power = 0.0000 mW

```


Figure 8.9. LaserMOD simulated modal power contributions with device bias at current threshold. Higher order modes contribute more power.

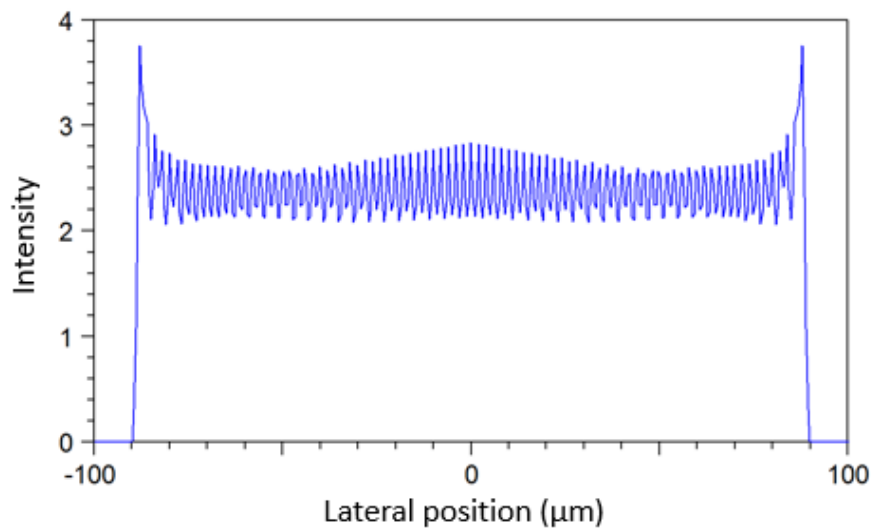


Figure 8.10. LaserMOD simulated slow axis near field under 4 amps bias. Peaks at edges due to carrier build up in simulation.

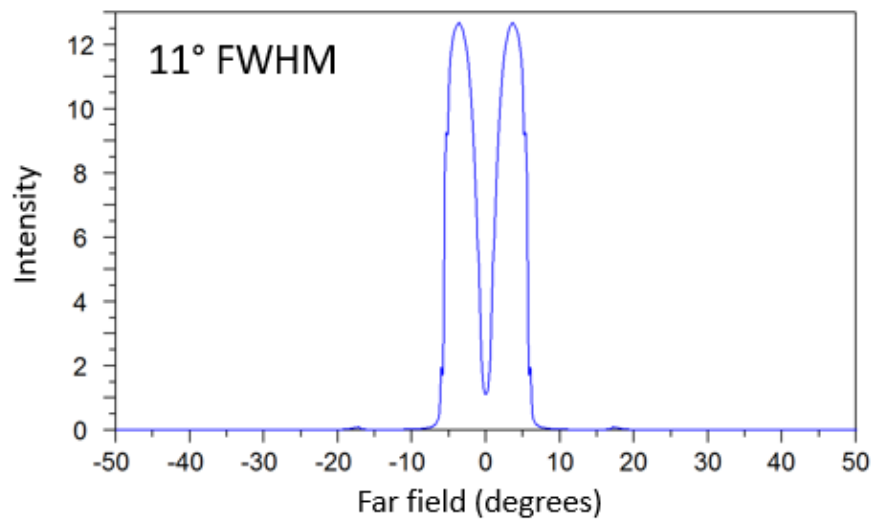


Figure 8.12. LaserMOD simulated slow axis far field under 4 amps bias. Slow axis bloomed as expected and full width half max matches test data. Intensity profile still has an unphysical dip in the center.

8 References

1. Winterfeldt M, Crump P, Wenzel H, Erbert G, Tränkle G. Experimental Investigation of Limits to Slow Axis Beam Quality in High Power Broad Area Diode Lasers. ; 2014.
2. Rauch S, Wenzel H, Radziunas M, Haas M, Tränkle G, Zimer H. Impact of longitudinal refractive index change on the near-field width of high-power broad-area diode lasers. *Appl Phys Lett*. 2017;110:263504.
3. Winterfeldt M, Rieprich J, Knigge S, Maaßdorf A, Hempel M, Kernke R, et al. Assessing the influence of the vertical epitaxial layer design on the lateral beam quality of high-power broad area diode lasers. ; 2016.
4. Stohs J, Bossert DJ, Gallant DJ, Brueck SRJ. Gain, refractive index change, and linewidth enhancement factor in broad-area GaAs and InGaAs quantum-well lasers. *IEEE J Quant Electron*. 2001;37(11):1449-59.
5. Wenzel H, Dallmer M, Erbert G. Thermal lensing in high-power ridge-waveguide lasers. *Opt Quant Electron*. 2008;40(5):379-84.
6. Piprek J. Self-consistent analysis of thermal far-field blooming of broad-area laser diodes. *Opt Quant Electron*. 2012;45.
7. Piprek J, Simon Li ZM. On the importance of non-thermal far-field blooming in broad-area high-power laser diodes. *Appl Phys Lett*. 2013;102(22).
8. Bennett BR, Soref RA, Del Alamo JA. Carrier-induced change in refractive index of InP, GaAs and InGaAsP. *IEEE Journal of Quantum Electronics*. 1990;26(1):113-22.
9. Hakki B,W., Paoli T. Gain spectra in GaAs double-heterostructure injection lasers. *J Appl Phys*. 1975;46:1299-306.
10. Crowley M, Houlihan J, Piwonski T, O'Driscoll I, Williams D,P., O'Reilly EP, et al. Refractive index dynamics of InAs/GaAs quantum dots. *Appl Phys Lett*. 2013;103:021114.
11. Rieprich J, Winterfeldt M, Tomm J, Kernke R, Crump P. Assessment of factors regulating the thermal lens profile and lateral brightness in high power diode lasers. ; 2017.

12. Lang RJ, Larsson AG, Cody JG. Lateral modes of broad area semiconductor lasers: theory and experiment. *IEEE Journal of Quantum Electronics*. 1991;27(3):312-20.
13. Coldren LA, Corzine SW, Mašanović ML. *Diode Lasers and Photonic Integrated Circuits*. 2nd ed. New Jersey: John Wiley & Sons, Inc.; 2012.
14. Agrawal GP, Dutta NK. *Semiconductor Lasers*. 2nd ed. Boston/Dordrecht/London: Kluwer Academic Publishers; 1993.
15. Henry CH, Logan RA, Bertness KA. Spectral dependence of the change in refractive index due to carrier injection in GaAs lasers. *J Appl Phys*. 1981;52(7):4457-61.
16. Soref RA, Bennett BR. Carrier refraction in quantum well waveguides. *Appl Opt*. 1989;28(17):3577.
17. Wenzel H, Crump P, Ekhteraei H, Schultz C, Pomplun J, Burger S, et al. Theoretical and experimental analysis of the lateral modes of high-power broad-area lasers. ; 2011.
18. Piprek J. Self-Consistent Far-Field Blooming Analysis for High-Power Fabry-Perot Laser Diodes. *Proc SPIE Int Soc Opt Eng*. 2013;8619:10.
19. Chow WW, Koch SW. *Semiconductor-laser Fundamentals: Physics of the Gain Materials*. 1st ed. Berlin: Springer; 1999.
20. Blood P. *Quantum Confined Laser Devices: Optical gain and recombination in semiconductors*. Oxford: Oxford University Press; 2015.
21. Pereira MFJ, Koch SW. Effects of Strain and Coulomb interaction on gain and refractive index in quantum-well lasers. *Journal of the Optical Society of America, Part B: Optical Physics*. 1993;10(5).
22. Hegarty S, Corbett B, Mcinerney J, Huyet G. Free-carrier effect on index change in 1.3 μm quantum-dot lasers. *Electron Lett*. 2005;41(7):1.
23. Murata S, Tomita A, Suzuki A. Influence of free carrier plasma effect on carrier-induced refractive index change for quantum-well lasers. *IEEE Photonics Technology Letters*. 1993;5(1).
24. Holonyak N, Kolbas R, Dupuis R, Dapkus P. Quantum-well heterostructure lasers. *IEEE J Quant Electron*. 1980;16(2):170-86.

25. Arakawa Y, Yariv A. Quantum well lasers--Gain, spectra, dynamics. *IEEE J Quant Electron*. 1986;22(9):1887-99.
26. Asada M, Kameyama A, Suematsu Y. Gain and intervalence band absorption in quantum-well lasers. *IEEE J Quant Electron*. 1984;20(7):745-53.
27. Stern F. Dispersion of the Index of Refraction Near the Absorption Edge of Semiconductors. *Phys Rev*. 1964;133(6):A1653-64.
28. Hall DC, Surette MR, Goldberg L, Mehuys D. Carrier-induced lensing in broad-area and tapered semiconductor amplifiers. *IEEE Photonics Technology Letters*. 1994;6(2):186-8.
29. Bawamia A, Eppich B, Paschke K, Wenzel H, Schnieder F, Erbert G, et al. Experimental determination of the thermal lens parameters in a broad area semiconductor laser amplifier. *Appl Phys B*. 2009;97(1):95-101.
30. Crump P, Böldicke S, Schultz CM, Ekhteraei H, Wenzel H, Erbert G. Experimental and theoretical analysis of the dominant lateral waveguiding mechanism in 975 nm high power broad area diode lasers. *Experimental and theoretical analysis of the dominant lateral waveguiding mechanism in 975 nm high power broad area diode lasers*. 2012;27(4):045001.
31. Nash FR. Mode guidance parallel to the junction plane of double-heterostructure GaAs lasers. *J Appl Phys*. 1973;44(10):4696-707.
32. Rees P, Blood P. Derivation of gain spectra of laser diodes from spontaneous emission measurements. *IEEE J Quant Electron*. 1995;31(6):1047-50.
33. O'Driscoll I, Piwonski T, Houlihan J, Huyet G, Manning R, Corbett B. Phase dynamics of InAs/GaAs quantum dot semiconductor optical amplifiers. *Appl Phys Lett*. 2007;91(26).